DIRECTIONALLY SENSITIVE NEUTRON DETECTOR FOR HOMELAND SECURITY APPLICATIONS

A Thesis

by

GRANT REID SPENCE

Submitted to the Office of Graduate Studies of
Texas A&M University
in partial fulfillment of the requirements for the degree of

MASTER OF SCIENCE

December 2011

Major Subject: Nuclear Engineering

Directionally Sensitive Neutron Detector for Homeland Security Applications

DIRECTIONALLY SENSITIVE NEUTRON DETECTOR FOR HOMELAND SECURITY APPLICATIONS

A Thesis

by

GRANT REID SPENCE

Submitted to the Office of Graduate Studies of
Texas A&M University
in partial fulfillment of the requirements for the degree of

MASTER OF SCIENCE

Approved by:

Chair of Committee,	William S. Charlton
Committee Members,	Pavel Tsvetkov
	Gary M. Gaukler
Head of Department,	Raymond Juzaitis

December 2011

Major Subject: Nuclear Engineering

ABSTRACT

Directionally Sensitive Neutron Detector for Homeland Security Applications.

(December 2011)

Grant Reid Spence, B.S., Texas A&M University

Chair of Advisory Committee: Dr. William S. Charlton

With an increase in the capabilities and sophistication of terrorist networks worldwide comes a corresponding increase in the probability of a radiological or nuclear device being detonated within the borders of the United States. One method to decrease the risk associated with this threat is to interdict the material during transport into the US. Current RPMS have limitations in their ability to detect shielded nuclear materials. It was proposed that directionally sensitive neutron detectors might be able to overcome many of these limitations.

This thesis presents a method to create a directionally sensitive neutron detector using a unique characteristic of ^{10}B. This characteristic is the Doppler broadening of the de-excitation gamma-ray from the $^{10}B(n,\alpha)$ reaction. Using conservation principles and the method of cone superposition, the mathematics for determining the incoming neutron direction vector from counts in a boron loaded cloud chamber and boron loaded semiconductor were derived.

An external routine for MCNPX was developed to calculate the Doppler broaden de-excitation gamma-rays. The calculated spectrum of Doppler broadened de-excitation gamma-rays was then compared to measured and analytical spectrums and matched with a high degree of accuracy.

MCNPX simulations were performed for both a prototype ^{10}B loaded cloud chamber and prototype ^{10}B loaded semiconductor detector. These simulations assessed the detectors' abilities to determine incoming neutron direction vectors using simulated

particle reactant data. A sensitivity analysis was also performed by modifying the energy and direction vector of the simulated output data for $^{7}Li^{*}$ particles. Deviation coefficients showed a respective angular uncertainty of 1.86° and 6.07° for the boron loaded cloud chamber and a boron loaded semiconductor detectors. These capabilities were used to propose a possible RPM design that could be implemented.

ACKNOWLEDGEMENTS

I would like to thank my advisor, Dr. William Charlton, for all his time and help in doing this research. Without him, I would probably be pursuing an MBA somewhere. Thanks are also due to my committee members, Pavel Tsvetkov and Gary Gaukler.

I would also like to thank my parents for being so awesome and supportive of my endeavor to become a lifelong student. Thanks are also due to Katie Putman for helping me with my edits.

"Life's a Garden. Dig it."

NOMENCLATURE

BF_3	Boron Tri-fluoride
B_4C	Boron Carbide
CCD	Compton Camera Detector
DHS	Department of Homeland Security
DNDO	Domestic Nuclear Detection Office
DOD	U.S. Department of Defense
DOE	U.S. Department of Energy
DOS	U.S. Department of State
DPRK	Democratic Peoples Republic of Korea
DSTO	Database on Nuclear Smuggling, Theft, and Orphan Radiation Sources
ECC	Emulsion Cloud Chamber
HEU	Highly Enriched Uranium
HPGe	High Purity Germanium
IAEA	International Atomic Energy Agency
ICBM	Intercontinental Ballistic Missile
ITDB	Illicit Trafficking Database
KAERI	Korean Atomic Energy Research Institute
MC	Monte Carlo Mathematical Model
MCNPX	Monte Carlo N- Particle Extended
NaI	Sodium Iodide
PMT	Photomultiplier Tube
PTRAC	Particle Tracing Function of MCNPX
PVT	Polyvynal Taluene
RPMs	Radiation Portal Monitor
SNM	Special Nuclear Material
US	United States

TABLE OF CONTENTS

Page

CHAPTER Page

LIST OF FIGURES

Page

Page

LIST OF TABLES

Page

CHAPTER I

INTRODUCTION

I.A. Motivation

I.A.1. Increased Threat for Nuclear Attack

The terrorist attacks on the United States in September of 2001 heightened concerns with regard to critical infrastructure security and the methods necessary for guaranteeing the safety of the general public.[1] Many of the events preceding the attacks on the World Trade Center in 2001 were unavoidable without the necessary framework to prevent them. Immediately following these attacks, the US undertook the task of improving its national security framework. The first step in improving the US framework came through gathering intelligence, both foreign and domestic, about likely future attacks. Among the various options for attack, the use of a nuclear device was deemed a probable threat.[1]

In order to maximize the effectiveness of the US's nuclear security framework, it is important to identify the parties which have the motive and capability to smuggle nuclear material across US borders. The two groups with the greatest probability of smuggling nuclear material into the US are state actors and terrorist/criminal organizations. If a state actor were to launch a conventional nuclear strike against the US, the probability that state actor would survive a US response would be very small. Therefore, it would be in a state actor's best interest to deliver the proposed nuclear device via covert methods such as vehicular smuggling. Unlike state actors, most terrorist organizations do not have the inherent capabilities to orchestrate a nuclear attack due to their lack of access to nuclear material, however, the nuclear threat these organizations pose is still viable. If a terrorist organization were to cooperate with a transnational crime syndicate, one with access to black market nuclear material, the likelihood of a terrorist attack increases.

This thesis follows the style of *Nuclear Technology*.

Nuclear material arrives on the black market through a complex network of sophisticated insider conspiracies at nuclear facilities.[2] Through this complex network, the IAEA's ITDB contains 540 confirmed incidents involving illicit trafficking of nuclear and radioactive materials since January 1, 1993.[3] This number only includes government-confirmed information. Bridging government-confirmed cases with open-source information, the DSTO contains a total of 1,440 cases of illicit nuclear smuggling during the period of 1991-2005.[4] Although the number of reported cases[3] of smuggled SNM since the mid 1990's is only 14, it is important to note that any weapon containing nuclear material will have devastating consequences. Furthermore, resourceful and powerful organized crime groups in Russia, Central Asia, the Caucasus, and Eastern and Southern Europe have established smoothly running mechanisms for smuggling drugs and weapons that could be easily adapted to nuclear material trafficking.[5] Couple this with recent claims that interactions between international terrorists and organized criminal groups are increasing[6], and the likelihood of an adversary attempting to smuggle nuclear material across US borders is seemingly inevitable.

I.A.2. Nuclear Security and the History of RPMs

Nuclear security can be defined as "the prevention of, detection of, and response to, theft, sabotage, unauthorized access, illegal transfer or other malicious acts involving nuclear and radiological material and their associated facilities.[7]" Nearly six decades ago when the United States was becoming aware of a probable nuclear proliferation threat it began enacting measures to increase nuclear security worldwide. One such example of US determination to increase nuclear security was in 1994 when Congress appropriated about $800 million for nuclear security efforts, including about $500 million to DOE, DOD, and DOS for international efforts.[1] As a result, RPMs were initially placed at ports of entry, air ports, railways, and vehicle border crossing locations overseas with the purpose of interdicting smuggled nuclear material. These RPMs consisted of several ^{3}He tubes surrounded in polyethylene for neutron detection, and plastic scintillators for gamma-ray detection. Eventually these RPM detectors were installed at US border locations to impede covert nuclear material from entering the US. The technology used

to create these RPM detectors was developed and benchmarked in the 1970's, thus the strengths and more importantly the limitations of these systems have been well documented. An intelligent adversary armed with the knowledge of these detector limitations consequently decreases the effectiveness of installed RPMs. Although the idea of having a successful network of effective RPMs is desirable, the current state of detector technology places this goal slightly out of reach. What the existing RPMs do provide, however, is a secure and robust network of detectors that provide the US government with a higher degree of risk management.

I.A.3. RPMs and Risk Management

"Risk is a function of the likelihood of an event and the consequence of that event.[8]" When looking at the possibility of preventing a nuclear incident in the US, there are various factors one must take into account. Among these factors, two stand out as the most important. The first is the party to which the nuclear incident can be held accountable. Before 9/11, the US government's perceived primary nuclear threat came from another state who would act through "conventional" means. Where the term "conventional" being defined as an open, broadcast, attack on the US by another state, or group of states, taking responsibility. For this reason the probability for a nuclear incident in terms of risk analysis was "aleatory (stochastic)[8]". After 9/11 and with the growing number of terrorist cells and regimes worldwide the threat of a nuclear incident has become multipolar. This multipolarity leads to "uncertainty in estimating the risk of a terrorist act" because it is "epistemic (state of knowledge) instead of aleatory (stochastic); for example, the adversary knows what acts will be attempted, but we as defender have incomplete knowledge to know those acts with certainty.[8]

The second factor to take into consideration is the means by which the nuclear device will arrive in the US. If a state decides to commit a nuclear attack on the US there is a very high probability that the device will be smuggled into the country to avoid US repercussions. Similarly, a terrorist organization would do everything in its power to covertly insert a nuclear device into the borders of the US and detonate it. Since World War II the US government has been developing methods of deterrence for an outright

conventional nuclear attack from a state, while conversely, the concept of preventing a covert nuclear incident is less developed. Some of the methods a state, or non-state, actor would use to smuggle a nuclear device into a country include: shipping it through a major port via cargo container, smuggling the device through an airport via a connecting flight from another country, smuggling the device in by railway from a connecting country, smuggling the device by personal watercraft or private airplane, smuggling the device through illegal border crossing, or smuggling the device in a vehicle across a border checkpoint. There are of course other means to which an adversary may covertly transport a nuclear device into the US; however, these are the primary areas of concern. At each of these locations: ports, railways, airports, and vehicle checkpoints, an RPM can be placed. It should be noted of course that at each location mentioned above the RPMs placed there are not identical to one another, but are instead very similar in their nuclear detection capabilities.

The concepts of risk, and risk management are instrumental to the allocation of protective resources by government agencies. As previously stated, risk can be defined as a function of the likelihood of an event and the consequence of that event occurring. Furthermore, the rate at which the risk of an event increases is proportional to the consequence of the event. When comparing relative risks for different types of attacks on the US, a nuclear attack has the greatest risk because the consequence of any nuclear attack is the most devastating. Since the consequence of a nuclear event is consistently devastating regardless of the scenario, the only way to decrease the risk of a nuclear event is to decrease the likelihood that event occurs. Along with physically protecting our borders from illicit nuclear material, the use of RPMs decreases the likelihood of a nuclear attack by psychologically decreasing the adversaries projected probability of success. If the adversary believes it is not possible to smuggle SNM over the border without getting caught, the probability that they will attempt to smuggle SNM is reduced, thus reducing the risk of an attack. Radiation detectors are placed at entrance points into the US to reduce the risk of nuclear threat with robust, proven and reliable detector technology. These characteristics encompass the RPMs in service today. If a

technological improvement were made on existing RPM detectors, the risk of a nuclear attack would decrease further.

I.B. Objectives

It is the goal of this research to develop a proof-of-concept for two prototype directionally sensitive RPMs. With the addition of directionality to the US's RPM detector network, the effectiveness of this network's ability to detect several difficult smuggling scenarios will drastically increase. The main steps in this research to create a new directionally sensitive RPM are outlined in the following subsections.

I.B.1. Benchmark Modeling

The effectiveness of existing RPMs was evaluated. An extensive model of a standard vehicle checkpoint RPM was modeled in MCNPX. Included in this model was a quantitative determination of an RPMs ability to detect SNM in a difficult HEU smuggling scenario.

I.B.2. Verifying the Phenomena of Doppler Broadening

A thorough analysis of the directional capabilities of ^{10}B was analyzed including how the phenomenon of a Doppler broadened de-excitation gamma-ray can provide directional information. Experimental measurements were given showing the existence of this Doppler broadened de-excitation gamma-ray. An analytical study was performed to determine the limits of this phenomenon. These analytical results were compared to the experimental results.

I.B.3. Simulations in MCNPX

Potential boron loaded detectors were simulated in MCNPX. Two boron based detectors were analyzed in these simulations. The first detector simulated was a BF_3 cloud chamber. In this simulation, PTRAC was used to print a list of information from the $^{10}B(n,\alpha)$ reaction occurring in the BF_3 cloud chamber. An algorithm was created that modified MCNPXs PTRAC output file to correctly Doppler broaden de-excitation

gamma-rays from the BF_3 cloud chamber simulation. These Doppler broadened gamma-rays were then compared with experimental results to determine the validity of the created algorithm.

The second detector modeled in MCNPX was a B_4C semiconductor detector. Various enrichment and detector geometry based simulations were performed in MCNPX to determine an ideal detector configuration. A vehicle-based simulation was performed similar to the RPM benchmark simulations. The de-excitation gamma-rays from this simulation were modified using the created Doppler broadening algorithm.

I.B.4. Inverse and Sensitivity Analysis

Using the results from the previous simulations, an inverse analysis was performed to determine the direction vector of the incoming neutron by combining conservation equations and mathematic principles with a modified Doppler broadened de-excitation gamma-ray. The Doppler broadened de-excitation gamma-ray was calculated using the Doppler broadening algorithm on detector simulation results in MCNPX. A sensitivity analysis was performed on the resultant neutron direction vector to determine the sensitivity to directional accuracy with small perturbations in the detector output.

CHAPTER II

BACKGROUND

II.A. An Analysis of Existing Radiation Portal Monitors

In this chapter we provide detail about deployed RPMs, as well as the detection capabilities of these RPMs.

II.A.1. Description of Current RPMs

An RPM is defined as an emplaced stationary detector where objects pass by the monitor and are screened for the presence of radioactive materials.[9] The ambiguity in the description of an RPM is due to its ability to be modified for various detection scenarios. Among these scenarios are cargo scanning, pedestrian scanning, vehicle scanning, and the scanning of railway cars. In each case the detection equipment may be different, however, the goal is the same: to detect radioactive particles emitted from radioactive sources. The primary objective for existing vehicle RPMs is to provide the initial screening of a vehicle or vehicles near its proximity therefore, the RPMs at border crossing locations are typically placed between lanes of traffic. Since the primary goal of these detectors is to scan large areas, the cross-sectional area of the RPM must be large in order to have as great a detection efficiency as possible. Examples of commercially available units are listed and shown in Table1 and Fig. 1 respectively.[10]

Table 1.

Commercially Available RPMs.[10]

Model	Manufacturer	Gamma Detector Type	Neutron Detector Type
CPM-VGN	Canberra	PVT	^{3}He
Guardian CRMS	NucSafe	PVT	^{3}He
Model 4500 VRM	Ludlum	PVT	^{3}He
AT-980 RPM	SAIC/Exploranium	PVT	^{3}He
PM 5000	Polimaster	PVT	^{3}He
VM-250AGN	TSA	PVT	^{3}He
RCD/2	RadComm	PVT	^{3}He
SGS-1500-GN	Thermo Scientific	PVT	^{3}He

Since the main function of RPMs is large-area, low-cost detection, there are a number of commercially available detector types that meet these requirements. The leading means used for photon detection is through the use of plastic scintillators which are almost exclusively PVT based because of its low cost and ease to manufacture. Other photon detector types could be used, such as HPGe semicondcutors, however they lack the ability to be mass deployed due to their cost of manufacturing. The typical choice for photon detection, NaI crystals, is not suitable for border monitoring applications because the time and budget needed to ensure the crystals grow the necessary size would become cost prohibitive.

The most commonly used method for detecting neutrons in RPMs is an array of ^{3}He embedded in some neutron moderator, particularly polyethylene. Although ^{3}He seems like an ideal candidate for neutron detection due its thermal neutron absorption cross section is 5330 barns[11], the White House decided in September 2009 that no new ^{3}He will be given to the production of RPMs due to an ongoing ^{3}He shortage.[12] For these reasons the DNDO is in search of a new type of neutron detector that is both efficient and cost effective.

Fig. 1. Vehicle RPMs at a border crossing checkpoint.[10]

II.A.2. Capabilities of Existing RPMs

As mentioned in the previous section, the primary goal of the DNDO is to place several low cost, high efficiency RPMs at vehicle crossing checkpoints. For these reasons, the DNDO has decided to proceed with reliable, well explored, detector technology that was created nearly four decades ago. This type of strategy has its benefits and drawbacks. The primary benefit is cost effectiveness. If the cost per unit is low enough the potential quantity of RPMs increases, thus increasing the overall detection probability for smuggled SIM. Another benefit to using well understood, pre-existing technology is that the limitations of the detector materials are known. Since the detection thresholds for PVTs and ^{3}He tubes are well documented from past experiments, border officials can create a complex network of RPMs which generate a high detection probability for most smuggling scenarios.

There are also several troubling elements with using low cost RPMs based off of time tested and verified technology. If an intelligent adversary were to have a working knowledge of the capabilities of the RPMs in service, it could be possible for them to fool the detector by shielding their radioactive material, thus the probability of success

for a smuggling scenario would increase. One particular scenario that exemplifies this is the smuggling of shielded HEU into the US. In the summer of 2002 an ABC news team performed an intricate series of tests on currently deployed RPMs and found troubling results:

> In the summer of 2002 an ABC News unit successfully slipped a lead-lined steel pipe containing a 6.8-kilogram (15-pound) cylinder of depleted uranium (DU) past U.S. Customs and Border Protection by placing it inside a standard cargo container. This material is unsuitable for a weapon, but its chemical properties are nearly identical to those of HEU. Our organization, the Natural Resources Defense Council (NRDC), prepared the shielded cylinder. The ABC News crew placed the pipe in an ordinary suitcase and carried it on passenger trains from Vienna to Istanbul--a route chosen to simulate a terrorist journey. The news crew saw no radiation detection equipment along the way.
>
> On reaching Istanbul, the journalists placed the suitcase inside an ornamental chest, packed alongside crates of huge vases in a large metal shipping container that left Istanbul by ship on July 10. When the container arrived at Staten Island in New York, Customs officials, part of Homeland Security, targeted it as high risk, in part because of its origin, and flagged it for more thorough screening. The machine and its operators failed to sense the uranium.[13]

Another element to consider when looking at the capabilities of the RPM is its large detection efficiency. This is true only because the solid angle (the amount of the detectors surface an incoming particle sees) is so large. Experiments for neutron and gamma detection efficiencies have been performed comparing different detection materials to those used in RPMs. In regards to neutron detection, "the results show that neutron detection efficiency is larger for the [boron loaded] liquid scintillator than for the He-3 counter (note that the He-3 counter has 6 times larger volume and covers more than 5 times larger solid angle).[14]" These results show that if a different type of neutron detector were used in an RPM, the neutron detection efficiency could be drastically improved. Conversely, the PVTs used for gamma-ray detection in the RPMs had a greater total absolute efficiency(the ability of a detector to detect incoming gamma-rays) than other similar gamma-ray detectors, but had a marginally lower absolute peak

efficiency (the resolution which the gamma-rays energy is recorded) then other similar gamma-ray detectors.[15]

II.B. Previous Work in the Field of Directionally Sensitive Detectors

Before continuing research into the field of directionally sensitive radiation detectors, it is important to recognize research previously performed in the area. In the following subsections it will be shown that detectors have been developed which are capable of providing incoming particle direction. Some of the mechanisms with which these detectors derive this directionality include particle recoil, scintillation, and absorption or decay reactions. In this section a brief introduction and history into some of these detector configurations will be given.

II.B.1. Cloud Chambers

One of the first directional detectors developed was a variation of Wilson's Cloud Chamber called an Emulsion Cloud Chamber. "The ECC technique was first introduced in 1951 to study high-energy interactions in cosmic rays.[16]" An ECC is constructed by carefully aligning alternate layers of a strong nuclear absorber in a sensitive nuclear emulsion.[17] The procedure to locate "high energy events then consists of a systematic survey for electronic showers in one of the emulsions deep in the stack; if the plates are carefully aligned, it is then possible to trace the shower in succeeding and preceding emulsions[17]", therein making it "possible to see the trails left by high energy particles – [an ECC] provides an environment where the wake of [high energy particles] can be observed.[18]" Using the "wake", or momentum, of these radioactive particles, the direction of the incoming particle can be calculated.

Initially the momentum of charged particle calculations consisted of tedious manual measurements, whereas today it can be fully automated. The two automated methods to calculate the charged particles momentum are the "coordinate" (sometimes called the "sagitta") method and the "angular" method. Each method measures the deviations of the charged particles trajectory from a straight line on the basis of position

or angle.[19] A depiction of the "coordinate" method and the "angular" method is illustrated[16] in Fig. 2.

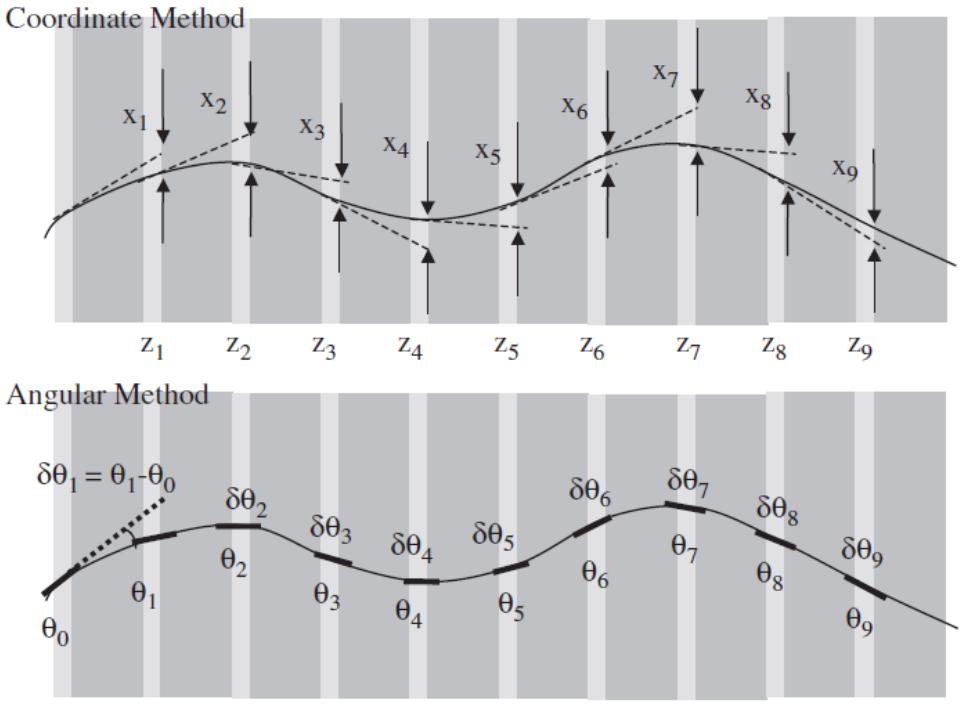

Fig. 2. A schematic overview of measuring multiple Coulomb scattering. The coordinate method requires precise alignment between emulsion plates, whereas angular method uses the angle difference between base tracks.

A similar cloud chamber detector configuration also currently exists that combines the neutron absorbing properties of ^{3}He, ^{4}He and ^{1}H, with the scintillation properties of CF_4 to provide directionality information about the incoming particle.[20] The detector consists of a chamber that contains CF_4 gas at low pressure for photon scintillation, one bar or ^{4}He is added to provide a recoil target for fast neutrons, and a few Torr of ^{3}He are added to detect thermal neutrons via the ^{3}He(n,p) reaction. Inside the canister also lies a cathode mesh and field cage which creates an electric field in an electron drift region. A charged particle created from one of the previously mentioned helium reactions then passes through the chamber leaving a trail of ionization electrons

in its wake. These electrons then drift to the amplification plane where an electron avalanche occurs; this is accompanied by the emission of scintillation light from CF_4. The scintillation light is then imaged by the CCD camera at the top of the canister. This detector configuration also has the added benefit of reducing the signal received from background radiation by adding track morphology cuts. A cross-sectional schematic of this detector configuration is illustrated[20] in Fig. 3, and alpha particle tracks are shown[20] in Fig. 4.

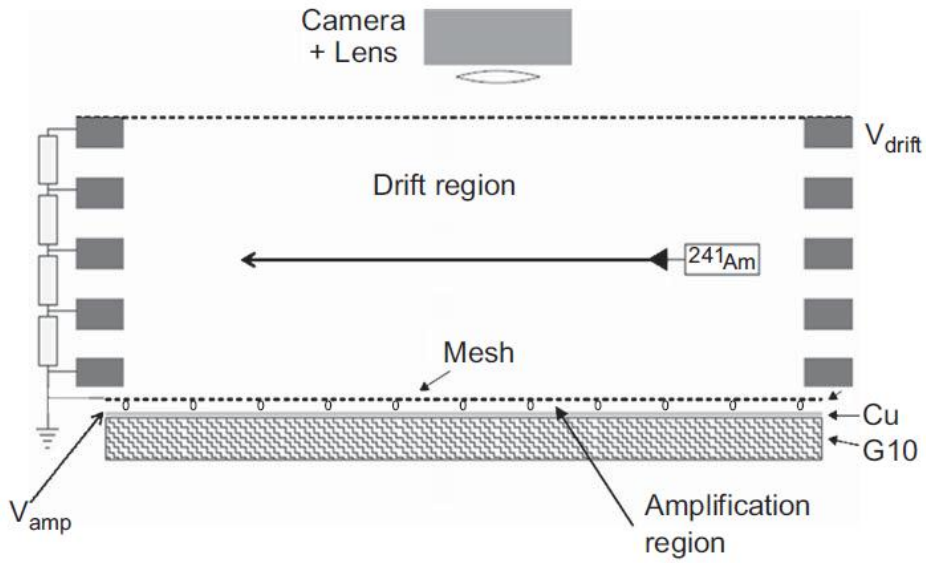

Fig. 3. Cross-sectional schematic of a gas combination cloud chamber neutron detector.

II.B.2. Compton Cameras

Another well developed directional detector system is a Compton camera. Although Compton cameras detect strictly photons, it is important to mention this detector configuration due to the magnitude of research performed in the area. Furthermore some of the mathematics behind Compton camera directionality applies directly to this research. A Compton scatter occurs when a photon scatters with a free electron orbiting a nuclei. The electron is ejected from its orbit taking away some of the

incident photons momentum, wherein the incident photon is then scattered to a different angle with a lower energy.[21]

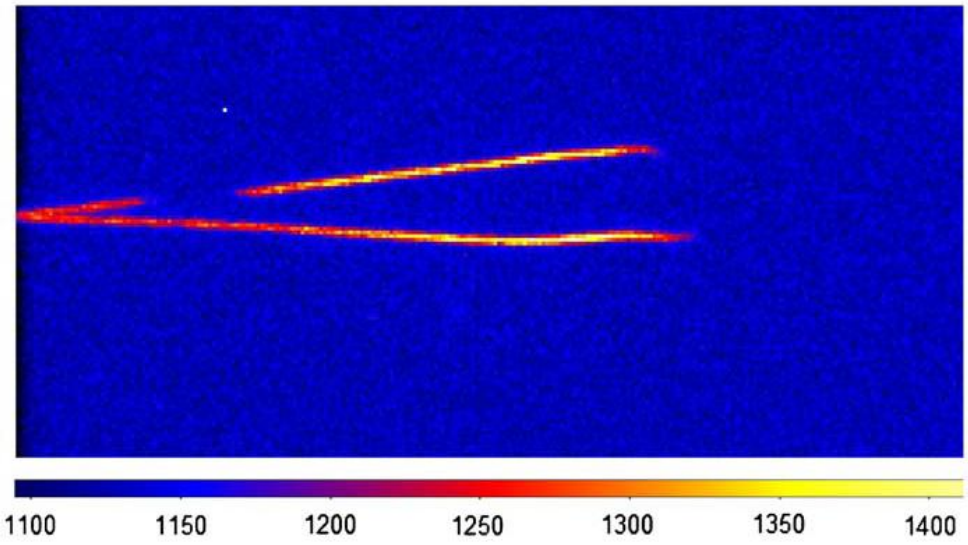

Fig. 4. Two alpha tracks from ^{241}Am source captured in the gas combination cloud chamber.

A Compton camera consists of a "combination of two separated gamma-ray detectors operated in coincidence… A collimated beam of gamma-rays is allowed to strike the first detector in which the desired mode of interaction is now Compton scattering. Some fraction of the scattered gamma-rays will travel to the second detector where they may also interact to give a second pulse. Because the separation distance is normally no greater than a few tens of centimeters, the pulses are essentially in time coincidence.[22] In order to recreate the incident photon's direction vector:

> It is the 2-site events that are of primary interest. In particular, if one could experimentally determine the position and energy at both interaction sites, one could then use the energy-angle relationship of Compton scattering to determine the Compton scattering angle. This angle then defines a cone of possible incident directions for the gamma-ray… Over many events, these cones, if projected onto an image plane or image sphere, will overlap at the source position, thus giving [the direction vector for the incoming photon].[23]

A visual representation of the angle reconstruction method[24] can be seen below in Fig. 5.

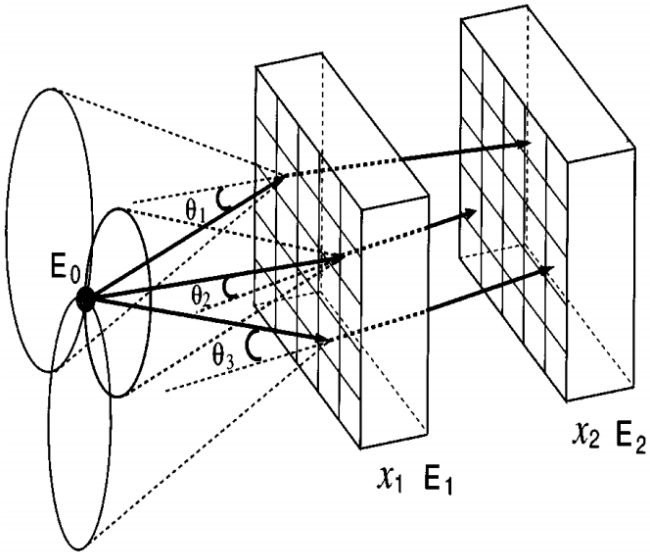

Fig. 5. A visual representation of the Compton Camera angle reconstruction method. E_0 is the source location, x_1 and x_2 are locations of the parallel gamma detectors.

II.B.3. Liquid Scintillator Detectors

Research has also been performed into using liquid scintillator detectors as directional detectors. Liquid scintillator detectors can provide particle directionality by both scintillation and recoil reactions. Along with directionality, a major benefit to using liquid scintillator detectors is their ability to detect both photons and neutrons. Before directional measurements can be made however, it is first necessary to separate photon counts from neutron counts.

Particle separation is done by using pulse shape discrimination. For the vast majority of organic scintillators, "the prompt fluorescence represents most of the observed scintillation light. A longer-lived component is also observed in many cases, however, corresponding to delayed fluorescence. [These can be dubbed] the fast and slow components of scintillation. Compared with the prompt decay time of a few nanoseconds, the slow component will typically have a characteristic decay time of several hundred nanoseconds. Because the majority of the light yield occurs in the prompt component, the long-lived tail would not be of great consequence except for one

very useful property: The fraction of light that appears in the slow component often depends on the nature of the exciting particle. One can therefore make use of this dependence to differentiate between particles of different kinds that deposit the same energy in the detector. This process is often called pulse shape discrimination and is widely applied to eliminate gamma-ray-induced events when organic scintillators are used as neutron detectors.[22]" Once separated by pulse shape discrimination, the scintillation tracks created by photons can be captured in CCD cameras, similar to the methods described in the cloud chamber section, to give particle directionality.

Liquid scintillators also give neutron directionality information in a similar manner to Compton cameras, this method is called the neutron double-scatter technique.[25] Similar to a Compton camera detector, "an incident neutron deposits energy in the first detector by scattering elastically from a proton in the detection material. The proton recoils with kinetic energy which is converted into detectable light that is read by PMTs and converted into an electrical pulse. The energy of the scattered neutron is determined by the time of flight between the first scatter and a subsequent scatter in a second detector. The original energy of the incident neutron and the scattering angle can be determined by employing energy and momentum conservation laws. The scattering angle defines a cone on the surface of which the neutron source must lie. Each new double-scatter event defines a new cone, the superposition of which determines the location of the neutron source.[26]" A better representation[26] of the phenomenon behind neutron double-scatter imaging can be seen in Fig. 6.

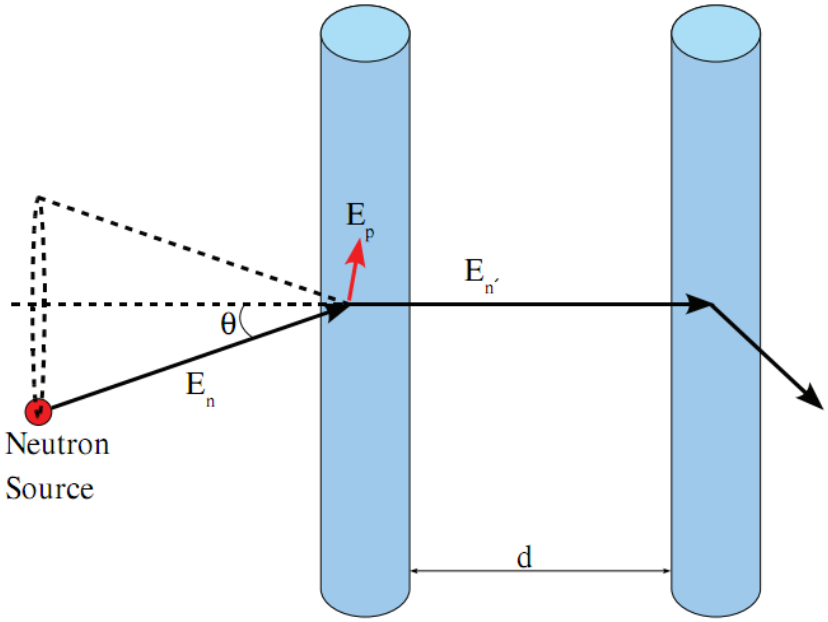

Fig. 6. Schematic of a neutron double-scatter imager.

II.B.4. Semiconductor Detectors

Recent research into semiconductor detector systems have allowed for extensive improvements in spatial resolution, high sensitivity, wide dynamic range and low noise.[27] Couple this with the already well known high detection efficiencies and improved energy resolution inherent in semiconductor detectors, and the concept of a position sensitive semiconductor detector is appealing. The one important caveat however is that since semiconductor detectors operate based off of charged particle ionizations, the probability for detecting neutrally charged neutrons is very low.[27] Therefore the surface of the pixilated semiconductor is coated with a thin layer of highly absorbing neutron material. The one requirement to making this semiconductor detector configuration a successful neutron detector is that the bi-products of the neutron reaction must include "heavy" charged particles, where a "heavy" particle is defined as a charged particle with a mass greater than an electron.[28] These charged particles then locally ionize electrons within the pixel in which they were generated. Stacking multiple coated semiconductor wafers on top of one another allows for directional recreation of the

charged particles through its interaction in each wafer's pixel. The incoming neutron vector can then be calculated through conservation principles.

The typical neutron absorbing semiconductor coating material is ^{6}LiF. The reactant particles created from the ^{6}Li(n,α) reaction are ^{3}H, and α, each carrying 2.7 MeV and 2.08 MeV respectively. Since the reactant products have such high energies the probability that they deposit most of their energy in localized depletion regions is low.[28] Simulations and experiments were performed to determine the coated semiconductors true detector efficiency using MCNPX and gave a detection efficiency of ~6%, where as the experimental results gave a detection efficiency of ~3%. A ~3% detection efficiency relates experimentally to 0.3 counts/pixel/second.[27] Results from coated semiconductor experiments show that if "heavy" particle detector efficiency can be increased, coated semiconductor detectors would be an ideal choice for a directionally sensitive neutron detector.

The existing RPM detector configurations outlined in this chapter have their benefits and detriments. They are robust and inexpensive, yet they are constructed with technology which allows for certain smuggling scenarios to go undetected. In this research the concept of adding directionality to RPMs to increase their detection capability is discussed. By combining the directional methods discussed in this chapter with the relatively unexplored phenomenon of Doppler broadening in the ^{10}B(n,α) reaction, a proof-of-concept for two prototype directionally sensitive RPM detectors was created.

CHAPTER III

THEORY

In this chapter the theory used to create a directionally sensitive neutron detectors using ^{10}B is discussed. The unique characteristics of the $^{10}B(n,\alpha)$ reactions is described in detail, and the Doppler broadening mathematics are analyzed. The basic principle of the Monte Carlo method and its application to MCNPX is given, and detail is also provided about how MCNPX can be used to simulate directionally sensitive neutron detectors.

III.A. $^{10}B(n,\alpha)$ Reaction

The 2.31 MeV Q value[22] of the $^{10}B(n,\alpha)$ reaction, and high energy reactant products make it a desirable material for detectors which operate based on ionization principles. When a neutron interacts with a ^{10}B atom it produces two secondary particles: a α and ^{7}Li particle. The unique feature of this reaction is that the ^{7}Li particle has a 94% probability of being created in an excited state.[22] If the reaction were to occur in the ground state, due to thermal neutron absorption, the energies of the reactant products are 1.02 MeV and 1.78 MeV for ^{7}Li and α respectively. If the $^{10}B(n,\alpha)$ reaction produces an excited state $^{7}Li^{*}$(where * represents an excited state), the $^{7}Li^{*}$ and ^{4}He products from thermal neutron absorption have energies of 840 keV (after de-excitation) and 1.47 MeV respectively. An illustrated[29] representation of the probabilities and energies for each reaction can be seen in Fig. 7. In order to de-excite, the $^{7}Li^{*}$ particle emits a 477.56 keV gamma-ray in flight. Since the de-excitation gamma-ray is emitted in flight, the energy of the de-excitation gamma-ray is modified by the kinetic energy and direction of the $^{7}Li^{*}$ particle. If the de-excitation gamma-ray is emitted in the same direction of the $^{7}Li^{*}$ particle, the energy of the gamma-ray appears greater than 477.56 keV in a photon detector. If the gamma-ray is emitted opposite the direction the $^{7}Li^{*}$ particle is traveling, the energy appears less than 477.56 keV. This is known as geometric Doppler broadening.

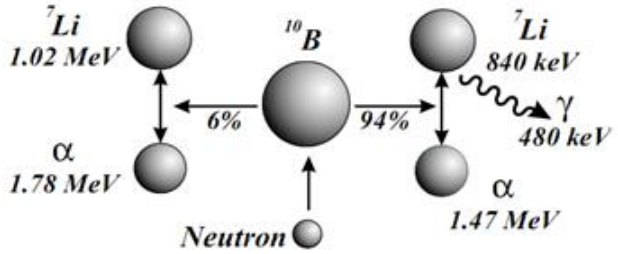

Fig. 7. The $^{10}B(n,\alpha)$ thermal neutron reaction showing the de-excitation 477.56 keV gamma-ray.

Another reason ^{10}B is desirable for a neutron detector is because of its large 3840 barn thermal neutron absorption cross-section.[30] This cross-section is inversely related to the incoming neutrons velocity.[31] This means that the neutron absorption cross-section in ^{10}B decreases with an increasing neutron energy as seen in Fig. 8.[32]

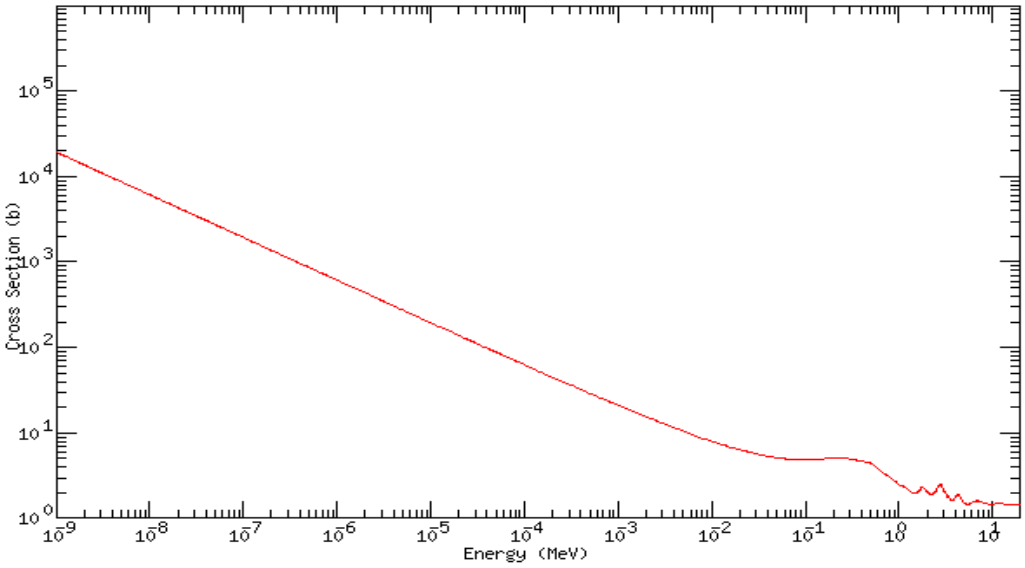

Fig. 8. Total neutron cross section for ^{10}B.

As part of the necessary parameters for the mathematics behind direction sensitive detectors, one of two quantities are needed before a directional analysis can be performed: the reactant product's energies or the reactant product's emission angles. In this research a forward model is defined as a scenario where the neutron energy, neutron

angle, and the reactant product's emission angles are known, leaving the reactant particle's energies to be solved. An inverse model is defined as a scenario where the reactant energies and angles of emission are known, leaving the incoming neutron energy and angle to be solved. Of course, in order to verify the accuracy of either model it is necessary to mathematically derive the incoming neutron energy (for verification of the inverse model), and the emission angles of the reactant products (for verification of the forward model). The tools used to derive these quantities are conservation of energy and momentum. If the ^{7}Li is left in an excited state, conservation of energy yields:

$$E_n = E_\alpha + E_{Li}^* - Q \tag{1}$$

If the ground state reaction occurs, conservation of energy yields:

$$E_n = E_\alpha + E_{Li} - Q \tag{2}$$

where E_n is the incoming neutron energy, E_α is the alpha particle energy, E_{Li}^* is the excited state $^{7}Li^{*}$ particle energy, E_{Li} is the ground state ^{7}Li particle energy, and Q is the Q-value of the reaction.

Conservation of momentum is then used to derive the angle between α and ^{7}Li, or θ and φ respectively, and the incident neutron direction vector. A visual representation of this can be seen in Fig. 9. The conservation of momentum in the x-direction yields:

$$\rho_n = \rho_{Li}\cos\varphi + \rho_\alpha\cos\theta \tag{3a}$$

Conservation of momentum in the y-direction yields:

$$0 = \rho_{Li}\sin\varphi - \rho_\alpha\sin\theta \tag{3b}$$

where ρ_n is the momentum of the neutron, ρ_{Li} is momentum of the ^{7}Li particle, ρ_α is the momentum of the alpha particle, φ is the angle between the ^{7}Li particle and the incident neutron direction, and θ is the angle between the α particle and the incident neutron.

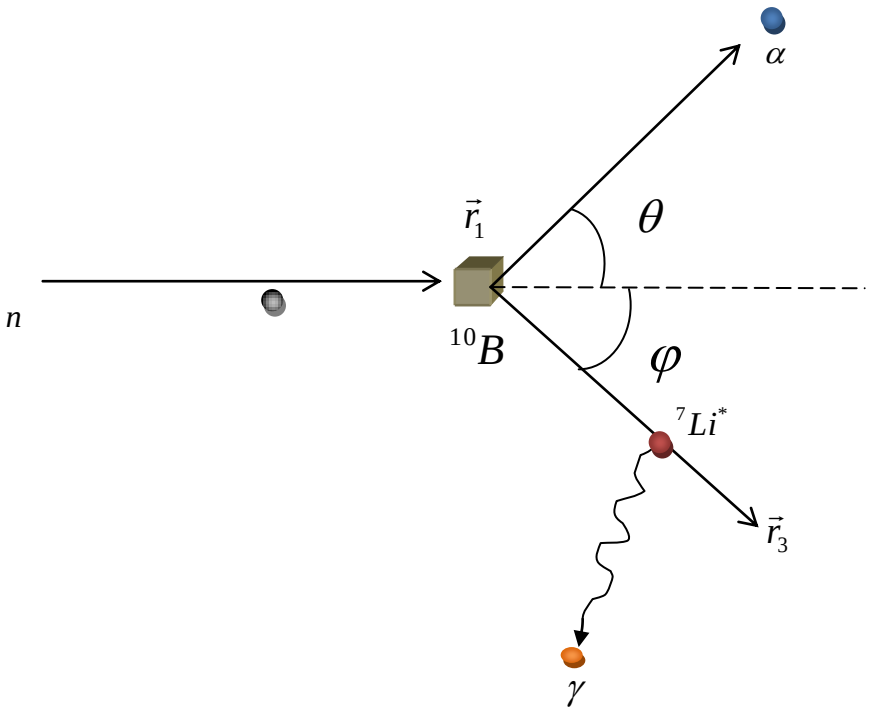

Fig. 9. Visual representation for the scattering angles of reactant products in the ^{10}B(n,α) reaction.

Subtracting $\rho_{Li}\cos\varphi$ from ρ_n in Equation 3(a), squaring both sides and rearranging yields:

$$0 = \rho_n^2 - 2\rho_n\rho_{Li}\cos\varphi + \rho_{Li}^2\cos^2\varphi - \rho_\alpha^2\cos^2\theta \quad (4)$$

Squaring Equation 3(b) yields

$$0 = \rho_{Li}^2\sin^2\varphi - \rho_\alpha^2\sin^2\theta \quad (5)$$

Subtracting Equation 4 from Equation 5 and solving for $\cos\varphi$ gives:

$$\cos\varphi = \frac{(-\rho_n^2+\rho_{Li}^2+\rho_\alpha^2)}{2\rho_{Li}\rho_n} \quad (6)$$

Substituting Equation 6 into Equation 3(a) and solving for $\cos\theta$ yields:

$$\cos\theta = \frac{\rho_n}{\rho_\alpha} + \frac{(\rho_\alpha^2-\rho_{Li}^2+\rho_n^2)}{2\rho_\alpha\rho_n} \quad (7)$$

Substituting the momentum-energy relation ($\rho = \sqrt{2mE}$) and Equation 2 into Equation 7, solving for θ gives:

$$\theta = \cos^{-1}\left[\frac{\left(2m_n\left(E_\alpha + E_{Li}^* - Q\right)\right)^{1/2}}{(2m_\alpha E_\alpha)^{1/2}} + \frac{2m_\alpha E_\alpha - 2m_{Li}E_{Li}^* - 2m_n\left(E_\alpha + E_{Li}^* - Q\right)}{2\left(2m_n\left(E_\alpha + E_{Li}^* - Q\right)\right)^{1/2}\left(2m_\alpha E_\alpha\right)^{1/2}}\right] \quad (8)$$

Substituting $\rho = \sqrt{2mE}$ and Equation 2 into Equation 6 and solving for φ gives:

$$\varphi = \cos^{-1}\left[\frac{-2m_\alpha E_\alpha + 2m_{Li}E_{Li}^* + 2m_n\left(E_\alpha + E_{Li}^* - Q\right)}{2\left(2m_n\left(E_\alpha + E_{Li}^* - Q\right)\right)^{1/2}\left(2m_{Li}E_{Li}^*\right)^{1/2}}\right] \quad (9)$$

where m_n, m_{Li}, and m_α are the masses of the neutron, $^7Li^*$ and α particles respectively, and E_α, E_{Li}^* are the energies of the respective α and $^7Li^*$ reactant particles. Equations 8 and 9 show that if the energy of the two reactant particles are determined experimentally in the detector system, the angle between the two particles can be calculated analytically. More importantly the angle of the neutron with respect to either the α or $^7Li^*$ particle can be determined. These experimental and analytical results can then be used in conjunction with the aforementioned forward and inverse models to recreate the unknown particle direction vectors. Note that Equations 8 and 9 can apply for both the case where the ^7Li particle is in an excited state (Equation 1) or in the ground state (Equation 2).

III.B. Doppler Broadening

Using Equations 8 and 9, we can acquire the neutron direction vector if we know the energies of the resultant products and the direction of one of the two resultant particles. We can acquire information about the direction of the $^7Li^*$ by observing the Doppler broadened energy of its de-excitation gamma-ray in a detector. We first determine if we can accurately predict the Doppler broadening effect using simulations compared to experiments.

Doppler energy broadening occurs when a particle is emitted from another particle that is already traveling at some velocity. Specifically, photon Doppler broadening occurs when some photons are emitted from particles moving towards the detector and others from particles moving away from the detector. This, in turn, affects the frequencies detected by the detector due to a Doppler effect. Some of the photons appear to have a frequency slightly greater than its original frequency and some a

frequency slightly less, depending on the direction and magnitude of the velocity of the emitting particles.[33] As previously mentioned, the $^{10}B(n,\alpha)$ reaction creates an excited state $^{7}Li^{*}$ particle 94% of the time. In order for the $^{7}Li^{*}$ particle to de-excite, it emits a 477.56 keV photon in flight. The thermal-neutron-induced, Doppler-broadened, de-excitation gamma-ray has been measured experimentally[34] and can be seen in Fig. 10. The experimental configuration consisted of a BF_3 chamber with cold neutrons incident from one direction on the chamber, and a HPGe set at 90° relative to the neutron beam for measuring the de-excitation gamma-rays.[34] As can be seen in Fig. 10, with a cold neutron (essentially zero energy) the de-excitation gamma-ray broadens from 477.56 keV to an approximate range of 469 keV to 486 keV.

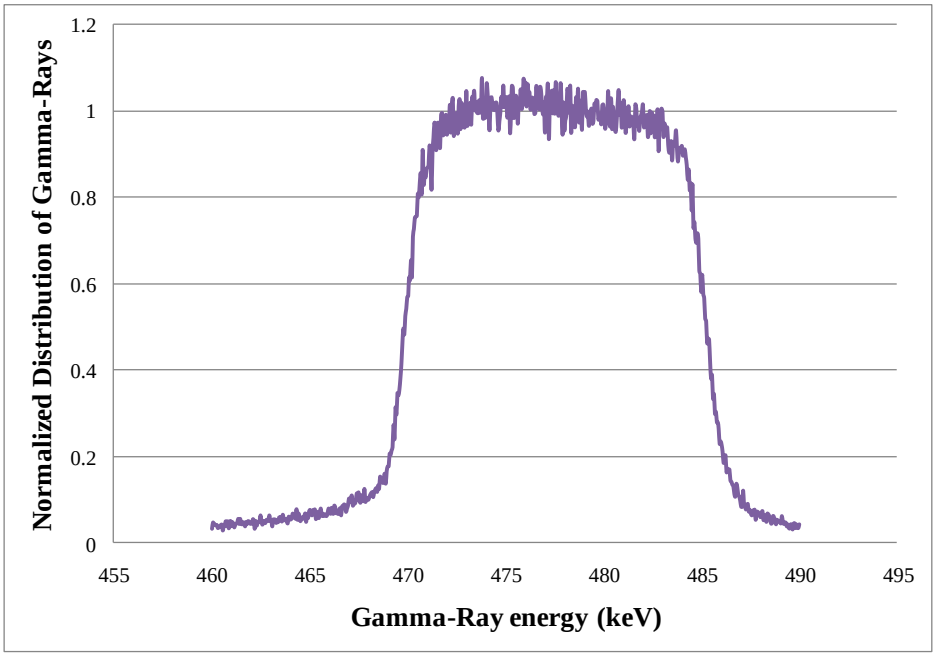

Fig. 10. Experimentally measured distribution of Doppler broadened photons from a thermally induced $^{10}B(n,\alpha)$ reaction.

The analytic solution to the Doppler broadened de-excitation gamma-ray is given by:

$$\nu_{\gamma}^{rel} = \frac{\nu_{\gamma}^{de}}{\frac{1}{\sqrt{1-\left(\frac{v_{Li}}{c}\right)}}} \frac{1}{\left(1-\frac{v_{Li}}{c}\cos\theta\right)} \tag{10}$$

where ν_{γ}^{rel} is the Doppler broadened gamma-ray frequency, ν_{γ}^{de} is the initial 477.56 keV de-excitation gamma-ray frequency, v_{Li} is the velocity of the $^{7}Li^{*}$ particle, c is the speed of light, and θ is the angle between the de-excitation gamma-ray and the $^{7}Li^{*}$ particle. The Doppler broadened gamma-ray frequency in Equation 10 can be analytically solved for all θ, such that $0 \leq \theta \leq \pi$. These results were compared to the experimental results in Fig. 11.

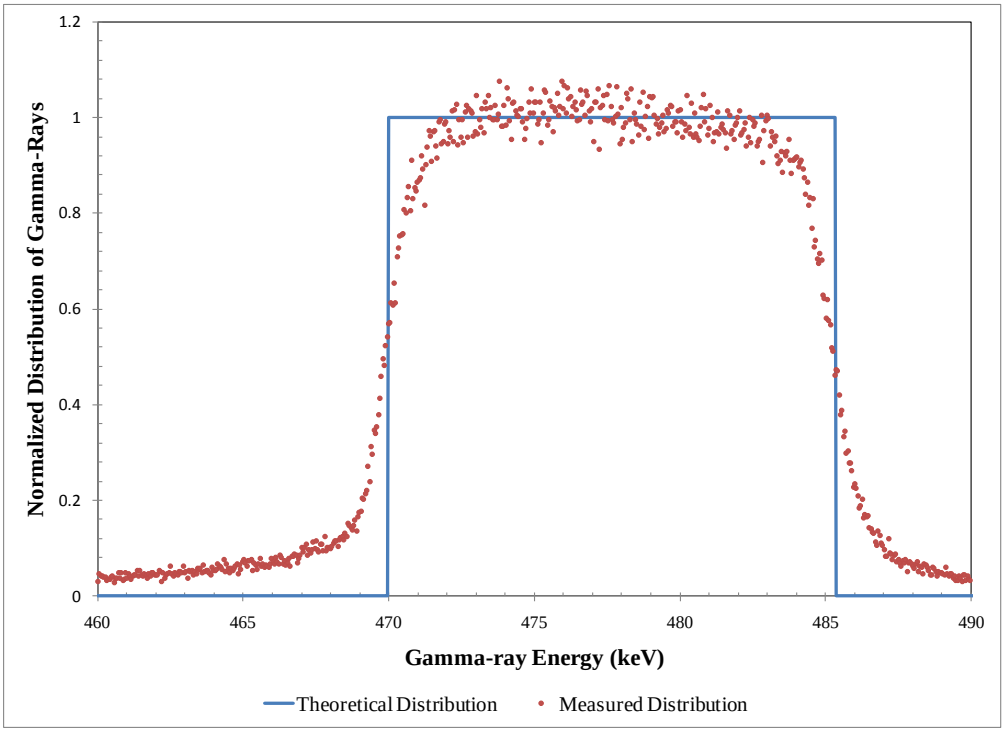

Fig. 11. Theoretical versus analytical Doppler broadened de-excitation photons from an excited $^{7}Li^{*}$ particle.

The disagreement between the analytic and measured distributions seen in Fig. 11 can be attributed to two factors in the experimental configuration. If the BF_3 gas were dense enough in the experimental configuration, the velocity of the $^{7}Li^{*}$ particle could theoretically decrease so fast, via scattering and ionization reactions in the BF_3, that its velocity contribution to the de-excitation gamma-ray would be significantly decreased. An experiment to verify this phenomenon was performed by measuring the Doppler broadened "hump" in three separately dense boron-containing materials, listed in

increasing density: BF_3 gas (~0.01 g/cm^3), a boric acid solution in water (~1.0 g/cm^3), and an NdFeB magnet (7.4 g/cm^3).[34] The results of this experiment can be seen in Fig. 12, it is important to note that as the density increases, the shape of the hump approaches the single 477.56 keV peak.

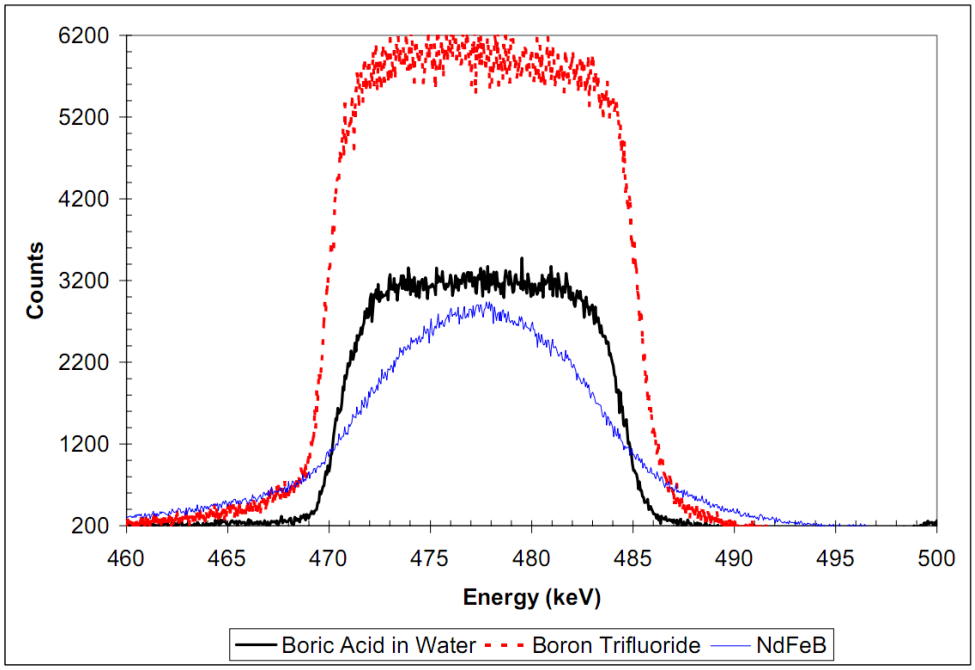

Fig. 12. Doppler broadened spectrum collected for three boron-containing materials showing the alternation of the ^{10}B(n,α) peak with material density.

The second factor which could affect the Doppler broadened photons in the experimental versus analytic results seen in Fig. 11 could be detector resolution. The Doppler broadened photons in the experimental configuration were detected using a HPGe detector with a measured resolution of 2.02 keV. Assuming a Gaussian shape to the peaks in the HPGe detector, the analytical results were modified to include detector resolution using:

$$f(x;\mu,\sigma) = \frac{1}{\sqrt{2\pi\sigma}} e^{\left(\frac{(x-\mu)^2}{2\sigma^2}\right)} \tag{11}$$

where x is the energy bin of the detector, μ is the mean of counts, and σ is the standard deviation due to the FWHM. The Gaussian error in the system was assumed to be

consistent with the broadened energy resolution calculated using the FWHM of the peaks. Fig. 13 compares the experimental Doppler broadened spectra, with the analytically calculated spectra including detector resolution. As seen in Fig. 13 , the detector resolution played a significant role in the shape of the Doppler broadened "hump". Furthermore, the similarities between the analytic and experimental results in Fig. 13 validate the accuracy of the Doppler broadening expressions given in Equation 10.

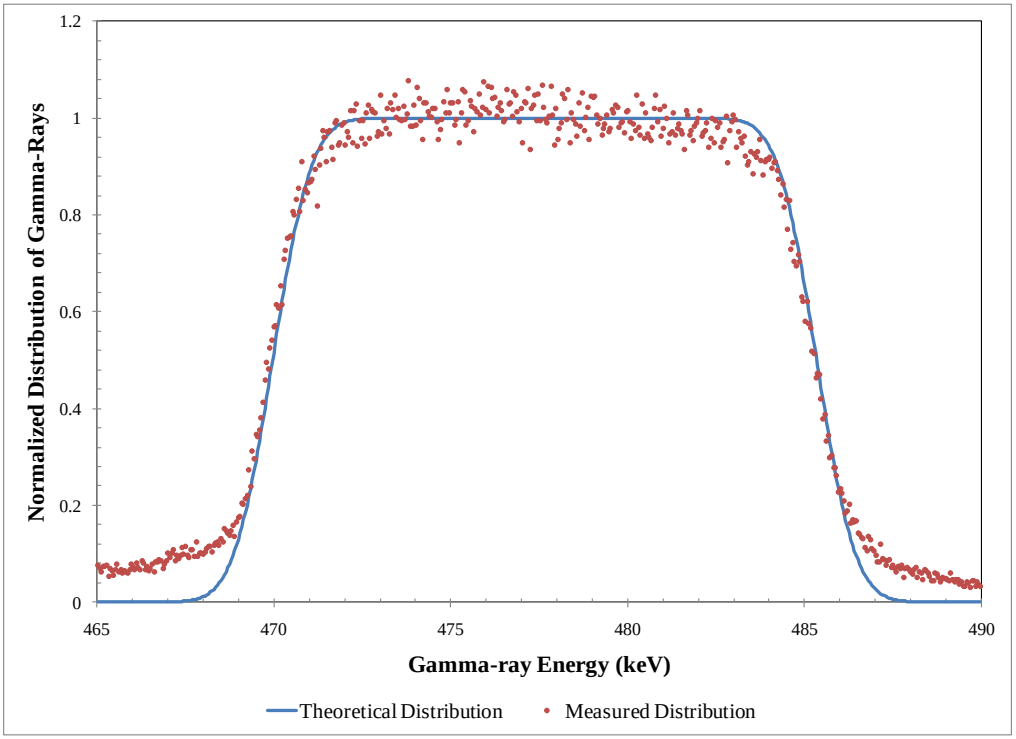

Fig. 13. Experimental results versus analytic solutions including detector resolution.

III.C. MCNPX, PTRAC, and the Monte Carlo Method

In this work, Monte Carlo (MC) simulations using MCNPX were used to model the interactions of neutrons with prototype directionally-sensitive neutron detectors. MCNPX is a code developed and maintained by Los Alamos National Laboratory that uses MC methods to simulate nuclear interactions. MCNPX uses the stochastic MC method to "obtain answers by simulating individual particles and recording some aspects

of their average behavior. The average behavior of the particles in the physical system is then inferred (using the central limit theorem) from the average behavior of the simulated particles.[35]" Typically, an MCNPX simulation operates by following each of many particles from a source throughout its life to its death in some terminal category (absorption, escape, etc.). To determine each step of the particle's life, probability distributions are randomly sampled.[35] Fig. 14 and the ensuing paragraph, paraphrased from the MCNPX manual[35], offer a greater explanation for the typical process MCNPX undergoes when simulating a particle history:

> [Fig. 14] represents the random history of a neutron incident on a slab of material that can undergo fission. Numbers between 0 and 1 are selected randomly to determine what (if any) and where interaction takes place, based on the rules (physics) and probabilities (transport data) governing the processes and materials involved. In this particular example, a neutron collision occurs at event 1. The neutron is scattered in the direction shown, which is selected randomly from the physical scattering distribution. A photon is also produced and is temporarily stored, or banked, for later analysis. At even 2, fission occurs, resulting in the termination of the incoming neutron and the birth of two outgoing neutrons and one photon. One neutron and the photon are banked for later analysis. The first fission neutron is captured at event 3 and terminated. The banked neutron is now retrieved and, by random sampling, leaks out of the slab at even 4. The fission-produced photon has a collision at event 5 and leaks out at event 6. The remaining photon generated at event 1 is now followed with a capture at event 7. Note that MCNPX retrieves banked particles such that the last particle stored in the bank is the first particle taken out.[35]

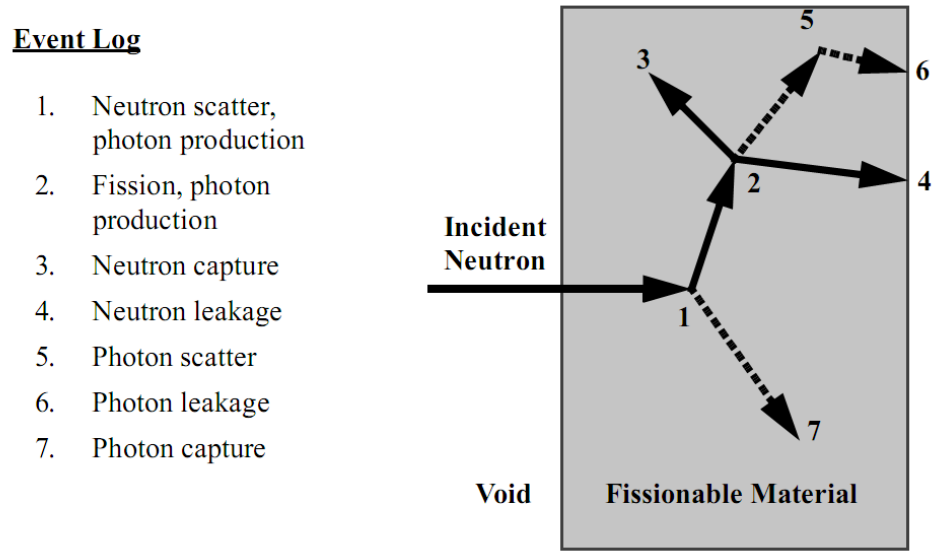

Fig. 14. MCNP event log for tracking a neutron's life in a fissionable material.

The MC method to determine a particle's history in a material has its advantages and disadvantages. One of the main advantages gained by using the MC method as compared to others is its computational efficiency, which can lead to increased simulation accuracy due to greater statistics as a result of more particle histories. More histories combined with an extensive knowledge of particle interaction probabilities makes MCNP simulations have an even higher degree of accuracy. The MC method however, does have a major disadvantage in the way it creates information for secondary reactant particles. Referencing back to Fig. 14, the neutron scatters at event 1, creating a photon that is "stored". After the remaining life of the neutron is carried out, MCNP gives information to the photon created at event 7 by sampling from a distribution of characteristic probabilities. In this scenario, since the photon is the only created particle, the characteristics, such as energy and angle, attributed to this photon only depend on the single scattering reaction at event 1. If event 1 were replaced with a $^{10}B(n,\alpha)$ reaction, however, the characteristics given to the $^{7}Li^{*}$ and α particles are incorrectly determined by considering only their dependence upon the characteristics of the incoming neutron. In order to appropriately model this reaction, the reactant products must be dependent on

one another as well as the incoming neutron. Thus, a complete simulation of a detector using ^{10}B would include using MCNP to model where neutrons interact in a detector with a $^{10}B(n,\alpha)$ reaction and then calculating the energies and angles of the resultant products using Equations 1, 8, 9, and 10. These calculated energies and angles could then be used to reconstruct incoming neutron direction cosines in simulated RPM detector configurations.

CHAPTER IV

INVERSE PROBLEM ANALYSIS

The steps outlined in Chapter III describe the mathematics necessary to calculate the energies and angles of reactant products from the $^{10}B(n,\alpha)$ reaction in a forward model given an incident neutron energy and direction. In order to solve for the incoming neutron direction in an actual detector system however, an inverse model is required. Described in the following subsections are the processes and mathematics behind deriving the incoming neutron direction vector through inverse modeling in a boron loaded cloud chamber, and a boron loaded semiconductor.

IV.A. Inverse Modeling of a Boron Loaded Cloud Chamber

As mentioned in Sec. II.B.1., cloud chambers have the unique ability to provide the energies and angles of reactant particles from the $^{10}B(n,\alpha)$ reaction. Listed in Table 2 are the pertinent known and unknown quantities necessary for the recreation of the incoming neutron direction vector interacting in a boron loaded cloud chamber.

Table 2.

Quantities Used to Solve Inverse Modeling in a Boron Loaded Cloud Chamber.

Measured Quantities	Known Quantities	Unknown Quantities
E_n	Q	$(u,v,w)_n$
E_α	$E_\gamma^{\text{de-excite}}$	
E_{Li}		
E^*_γ		
$(u,v,w)_\alpha$		
$(u,v,w)_{Li}$		
$(u,v,w)_\gamma$*		

(u,v,w): Direction cosine for the respective particle.

Using a combination of the measured and known quantities, and conservation of momentum in every direction, the direction cosine for the incoming neutron can be calculated. The quantities in Table 2 are used in conjunction with Equation 3(a) to give:

$$u_n = \frac{u_\alpha\left(\sqrt{2m_\alpha E_\alpha}\right)+u_{Li}\left(\sqrt{2m_{Li}E_{Li}}\right)}{\sqrt{2m_n E_n}} \tag{12}$$

$$v_n = \frac{v_\alpha\left(\sqrt{2m_\alpha E_\alpha}\right)+v_{Li}\left(\sqrt{2m_{Li}E_{Li}}\right)}{\sqrt{2m_n E_n}} \tag{13}$$

$$w_n = \frac{w_\alpha\left(\sqrt{2m_\alpha E_\alpha}\right)+w_{Li}\left(\sqrt{2m_{Li}E_{Li}}\right)}{\sqrt{2m_n E_n}} \tag{14}$$

where u_n, u_α, u_{Li}, are the respective direction cosines of the incoming neutron, α and ^{7}Li particles with respect to the x-axis; v_n, v_α, v_{Li}, are the respective direction cosines of the incoming neutron, α and ^{7}Li particles with respect to the y-axis; and w_n, w_α, w_{Li}, are the respective direction cosines of the incoming neutron, α and ^{7}Li particles with respect to the z-axis. In experimental conditions, the BF_3 cloud chamber detector provides the energies and angles of the $^7Li^*$ and α reactant particles. The angle and energy of the Doppler broadened de-excitation gamma-ray is recorded in coincidence in the adjoining HPGe detector. With reactant particle energies and directions, the incoming neutron direction cosines can be calculated via the mathematics in Equations 12-14.

Recreating the incoming neutron direction cosines from simulated MCNPX data required a slightly different method. Since MCNPX and PTRAC do not conserve particle information when generating ^{10}B(n,α) reactant particle data, Equations 12-14 cannot be used. In order to create the incoming neutron direction vector using the PTRAC data produced from MCNPX, information about the angle of emittance for one of the three reactant particles was manufactured. Since the incoming neutron information from the simulation was listed in PTRAC, Equations 12-14 could be modified to manufacture appropriate direction cosines for a reactant particle. In this research, the $^7Li^*$ particle information was held constant, and the alpha particle direction cosines were manufactured using:

$$u_\alpha = \frac{u_n\left(\sqrt{2m_n E_n}\right)+u_{Li}\left(\sqrt{2m_{Li}E_{Li}}\right)}{\left(\sqrt{2m_\alpha E_\alpha}\right)} \tag{15}$$

$$v_\alpha = \frac{v_n\left(\sqrt{2m_n E_n}\right)+v_{Li}\left(\sqrt{2m_{Li}E_{Li}}\right)}{\left(\sqrt{2m_\alpha E_\alpha}\right)} \quad (16)$$

$$w_\alpha = \frac{w_n\left(\sqrt{2m_n E_n}\right)+w_{Li}\left(\sqrt{2m_{Li}E_{Li}}\right)}{\left(\sqrt{2m_\alpha E_\alpha}\right)} \quad (17)$$

After calculating the direction cosine for the α particle, both reactant particles had energies and directions which obeyed the necessary conservation principles. Equations 13-15 were then used to calculate the incoming neutron direction vector. Although the concept of using the incoming neutron information and Equations 15-17 to manufacture α particle information seems redundant, the purpose of generating this data was to emulate experimental data of the $^{10}B(n,\alpha)$ reaction provided from a BF_3 detector. Using the methods provided in this subsection, an incoming neutron direction cosine can be reconstructed in simulated and experimental conditions.

IV.B. Inverse Modeling of a Boron Loaded Semiconductor

In detector configurations like a boron loaded semiconductor detector, the direction vectors for the α and ^{7}Li particles cannot be measured directly. Since the reactant particle direction vectors are unknown, the steps outlined in Sec. III.A. to calculate the angle between reactant products and the incoming neutron cannot be performed. Listed in Table 3 are the pertinent known and unknown quantities necessary for the recreation of the incoming neutron direction vector interacting in a boron loaded semiconductor.

Table 3.

Quantities Used to Solve Inverse Modeling in a Boron Loaded Semiconductor.

Measured Quantities	Known Quantities	Unknown Quantities
E_n	Q	$(u,v,w)_n$
E_α	$E_\gamma^{\text{de-excite}}$	$(u,v,w)_\alpha$
E_{Li}		$(u,v,w)_{Li}$
E^*_γ		
$(u,v,w)^*_\gamma$		

Although the direction cosines of the reactant particles are not given and cannot be calculated, solving for the angle between the de-excitation gamma-ray and the $^{7}Li^{*}$ particle can be done. Using this angle and the superposition of cones, it is possible to create a set of solutions in which the incoming neutron direction vector must lie. The first step in this process is to calculate the angle between the de-excitation gamma-ray and the $^{7}Li^{*}$ reactant particle. This is done by rearranging Equation 11 to solve the angle between the two particles:

$$\theta_{\gamma-\mathrm{Li}} = \cos^{-1}\left[\frac{c}{v_{\mathrm{Li}}}\left(1 - \frac{\nu_{\gamma}^{\mathrm{de}}}{\frac{1}{\sqrt{1-\left(\frac{v_{\mathrm{Li}}}{c}\right)}}}\frac{1}{\nu_{\gamma}^{\mathrm{rel}}}\right)\right] \tag{18}$$

where $\theta_{\gamma-\mathrm{Li}}$ is the angle between the de-excitation gamma-ray and the $^{7}Li^{*}$ particle. With the separation angle calculated, a surface equation for a cone of solutions including all possible $^{7}Li^{*}$ direction vectors can be created using the formula for a conic surface as seen in Equation 19:

$$S(u) = (u,v,w)_{\gamma^{*}} \cdot (u,v,w)_{\mathrm{Li}} - \cos\left(\theta_{\gamma^{*}\cdot\mathrm{Li}}\right) = 0 \tag{19}$$

where $S(u)$ denotes the surface of the cone formed by all possible $^{7}Li^{*}$ direction vectors. It is important to note that every vector lying on the surface of the cone defined by Equation 20 is a different $^{7}Li^{*}$ solution vector, each having their own individual neutron direction vector solution sets. After a solution set of all possible $^{7}Li^{*}$ direction vectors has been created, Equation 10 can be used to calculate the angle between the incoming neutron and one of the possible $^{7}Li^{*}$ direction vectors, or $\varphi_{\mathrm{n}\cdot\mathrm{Li}}$. The newly calculated $\varphi_{\mathrm{n}-\mathrm{Li}}$ now allows for the creation of another conic surface solution set which possesses the incoming neutron direction vector. The equation for this conic surface solution set is defined by Equation 20:

$$S(u) = (u,v,w)_{\gamma^{*}} \cdot (u,v,w)_{\mathrm{Li}} - (u,v,w)_{\mathrm{n}} \cdot (u,v,w)_{\mathrm{Li}} \tag{20}$$
$$-\cos\left(\theta_{\gamma^{*}\cdot\mathrm{Li}}\right) + \cos(\varphi_{\mathrm{n}\cdot\mathrm{Li}}) = 0$$

where $(u,v,w)_{\mathrm{n}}$, is the direction vector of the incoming neutron. Thus, it is important to note that using the process described above results in a space of solution sets for $(u,v,w)_{\mathrm{Li}}$ and $(u,v,w)_{\mathrm{n}}$ and not a single unique solution. In this work we will focus on

the ability to determine the $\theta_{\gamma^*\cdot Li}$ quantity and not consider in detail the superposition of cones problem (which is routinely solved in medical physics).

A visual representation of the steps taken to create the conic surfaces in Equations 19 - 20 are illustrated in Fig. 15 –Fig. 17. In Fig. 15 the neutron interacts with a ^{10}B nucleus at (0,0,0) causing a $^{10}B(n,\alpha)$ reaction which emits a $^{7}Li^{*}$ particle in the negative Y, and positive Z directions. Since this simulation occurs in a boron loaded semiconductor detector, only the $^{7}Li^{*}$ energy is detected in the system. Shortly after the initial $^{10}B(n,\alpha)$ reaction , the $^{7}Li^{*}$ particle emits it's de-excitation gamma-ray traveling in the positive X direction. Since both the angle and energy of this gamma-ray are detected by a secondary photon detector, the angle between the gamma-ray and the $^{7}Li^{*}$ can be calculated ($\theta_{\gamma^*\cdot Li}$). The direction vector of the de-excitation gamma-ray is then set as the axis of rotation, and a cone surface is created by rotating 2π around this axis at $\theta_{\gamma^*\cdot Li}$ as seen in Fig. 16.

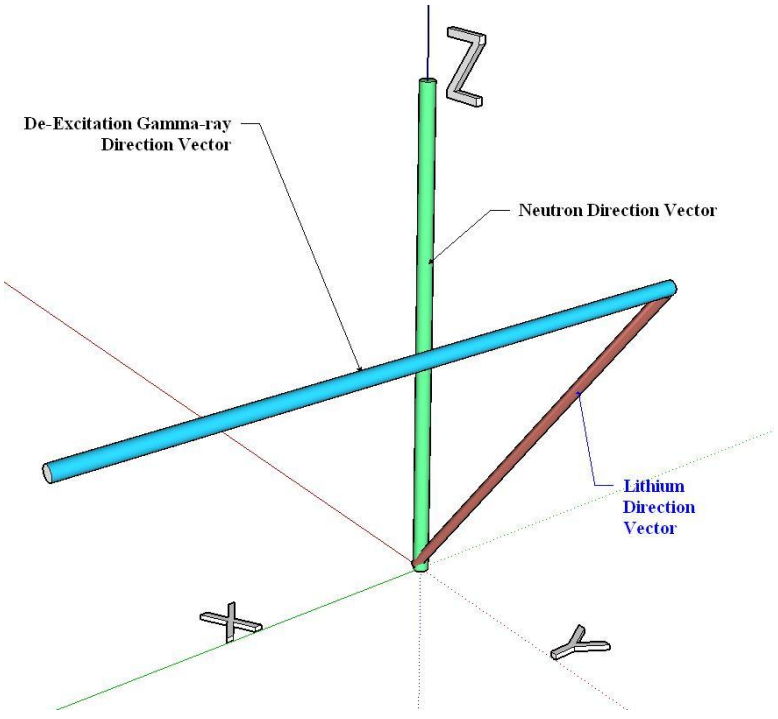

Fig. 15. A schematic illustrating an example of the direction vectors for the three particles of interest in the $^{10}B(n,\alpha)$ reaction.

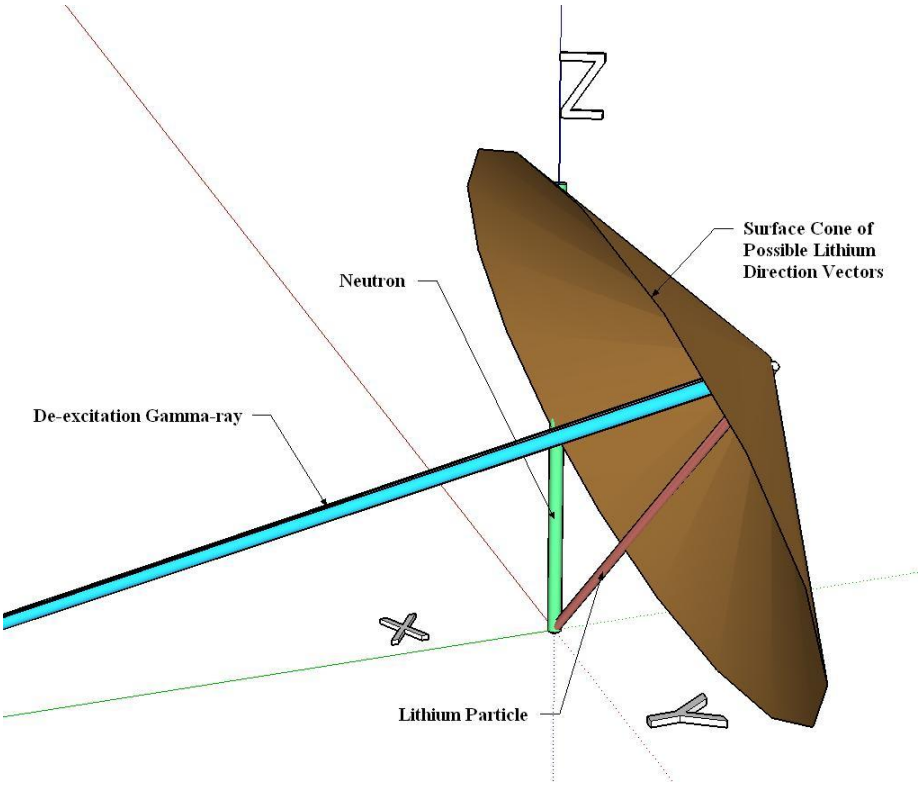

Fig. 16. A schematic illustrating the cone surface of possible $^{7}Li^{*}$ direction vectors from Equation 20.

From the surface of the cone displayed in Fig. 16, Equation 21 is used to generate a cone surface of incoming neutron direction vectors for every $^{7}Li^{*}$ direction vector. Included in the neutron direction vector cone surface is the direction the neutron came from (0,0,-1) as seen in Fig. 17. If a neutron source were emitting neutrons in a constant direction, several ^{10}B nuclei in the proximity of the first interaction site would also undergo the $^{10}B(n,\alpha)$ reaction. These subsequent reactions would create a similar series of secondary neutron surface cones similar to the cone seen in Fig. 17. An overlapping of multiple surface cone solutions can then be used to triangulate the original incoming neutron direction cosine as seen in Fig. 18. Using the method of cone superposition, if a prototype boron loaded RPM semiconductor detector were created, the incoming neutron direction cosines could be reconstructed.

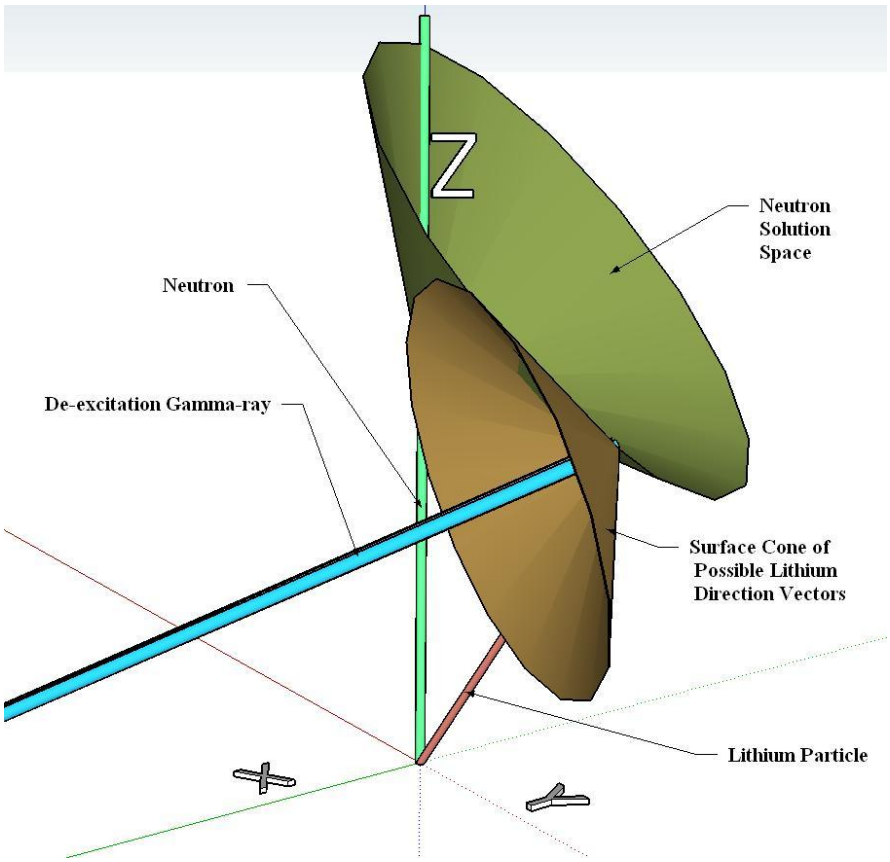

Fig. 17. A schematic illustrating the superpostition of cones to solve for the incoming neutron direction vector outlined in Equation 21.

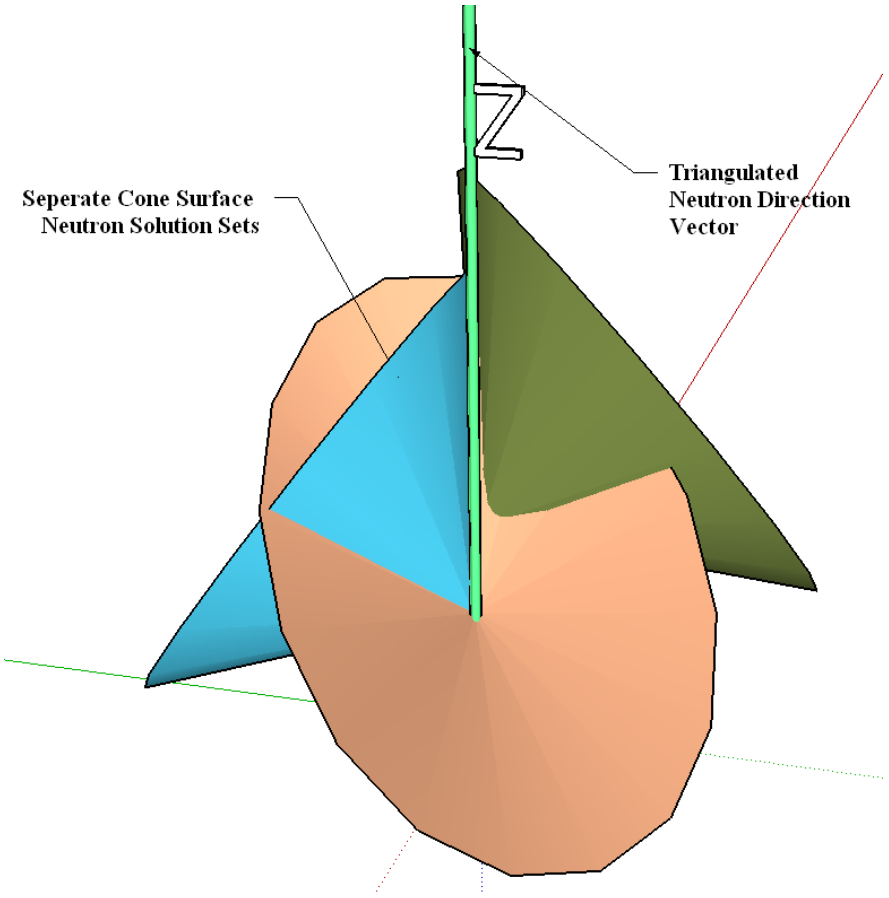

Fig. 18. The source of the incoming neutron direction vector can be determined by triangulating multiple neutron surface cones from interactions in close vicinity.

CHAPTER V

PROTOTYPE DESIGNS

V.A. Boron Loaded Cloud Chamber

In Sec. III.D.1 the concept of creating a directionally sensitive cloud chamber using ^{10}B was discussed. In this section, the feasibility of placing a boron loaded cloud chamber at vehicle monitoring stations will be analyzed. Currently the neutron detectors at vehicle monitoring stations consist exclusively of ^{3}He tubes. The performance of these ^{3}He tubes will be compared to similar tubes filled with BF_3 to determine the limits of either gas' detection capability, and then a prototype BF_3 cloud chamber will be introduced.

The thermal neutron capture cross section for ^{3}He tubes is 5327 barns which roughly doubles the 3840 barn cross section of BF_3. To further this, "since ^{3}He detectors can be operated at higher gas pressures, they theoretically offer higher detection efficiency than BF_3. However, ^{3}He detectors are more sensitive to gamma radiation and result in poor discrimination between thermal neutron pulses and gamma radiation pulses.[36]" A series of experiments were performed by Pacific Northwest National Laboratory comparing the ^{3}He tubes in RPMs to hypothetical BF_3 tubes of the same dimensions . The experiments were performed within the same environment (the material in the tubes were simply substituted), with a different number of tubes and different gas pressures. In the experiment a lead and polyethylene shielded ^{252}Cf source was placed two meters from the center of, and perpendicular to, the front face of the RPM. The results[37] of these tests are seen in Fig. 19.

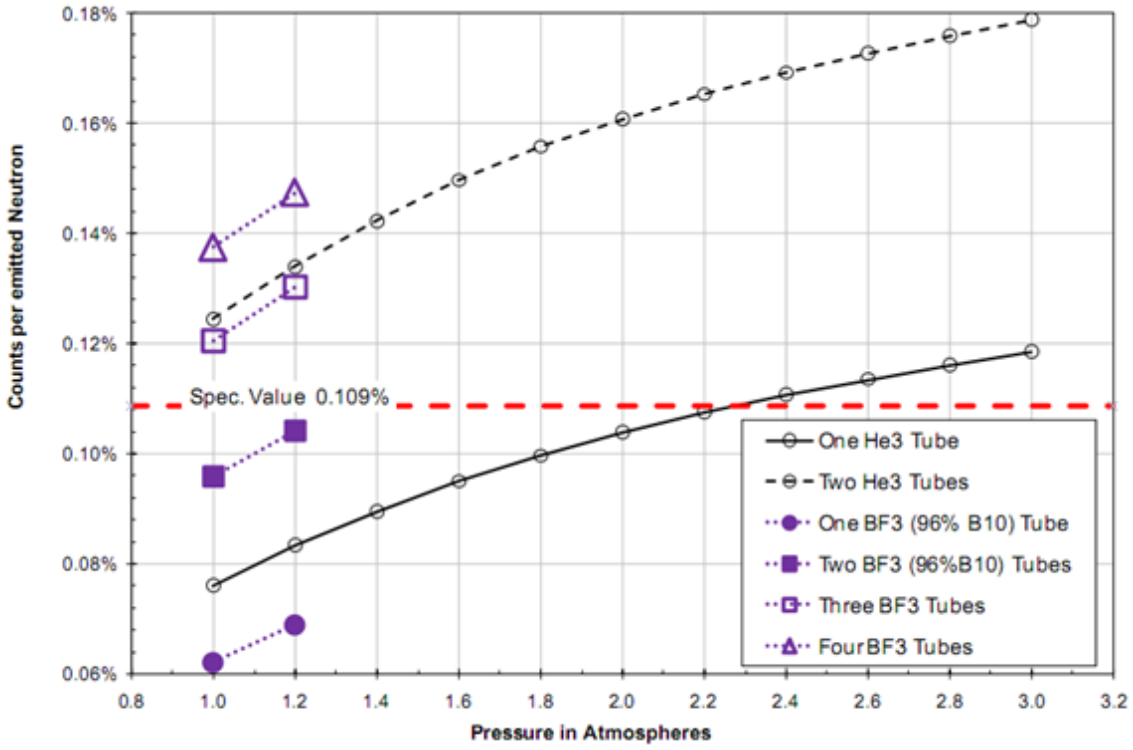

Fig. 19. Absolute detection efficiency for multiple ^{3}He and BF_3 tubes.[37]

As seen in Fig. 19, with a shielded source both of these detector configurations have a relatively low absolute efficiencies. It should be noted that a minimum of three BF_3 tubes are needed to meet the required efficiency of 0.109% at one atmosphere, and roughly two times the amount of BF_3 is needed to match or supersede the ^{3}He detection efficiency at a similar pressure. It is also important to note that BF_3 is not an ideal proportional counter gas, so the maximum allowed pressure in the detector is slightly above one atmosphere as seen in Fig. 19. Since the detector configuration is at such a low pressure, relative to ^{3}He tubes, a larger detector vessel containing BF_3 would be allowed without violating safety constraints.

The ideal prototype boron loaded cloud chamber for vehicle crossing check points would consist of: a large emulsion chamber like detector, similar to those referenced in Sec. II.B.1, containing BF_3 at 1.2 atmospheres surrounded completely by a series of HPGe detectors. In this configuration a neutron would enter the BF_3 vessel and

undergo a $^{10}B(n,\alpha)$ reaction. The reactant heavy charged particles would then create ionized tracks visible to the CCD, and the resulting de-excitation gamma-ray would be detected in the HPGe detectors surrounding the BF_3 well. The energy and angles for each of these reactant particles would be recorded, and the incoming neutron direction vector could be calculated via the methods mentioned in Sec. III.D.1.

V.B. Boron Loaded Semiconductor

In the previous section the proposed boron loaded cloud chamber used BF_3 gas as its main neutron detecting medium. BF_3 and other boron loaded gases have been developed and benchmarked for over three decades. Conversely a boron loaded semiconductor material that would meet the durability and efficiency requirements of RPMs does not currently exist. The neutron semiconductor detectors that do exist are of the coated and perforated semiconductor types mentioned in Sec.II.B.4. In this section the implementation of boron to these coated semiconductors will be analyzed, and a hypothetical, prototype, boron doped semiconductor detector for vehicle crossing stations will be introduced.

With a thin layer of ^{10}B deposited on the surface of a semiconductor, "the maximum thermal neutron detection efficiency for a single-coated planar device [is] 4.0%.[38]"The neutron absorption efficiency was found to be so low due to the lack of thickness of neutron absorbing ^{10}B, and a peeling and delamination of the coatings from thin-film stresses introduced by the evaporative disposition.[38] In order to increase the film adhesion to the device surface, tiny holes were etched into the diode barrier surface before applying the layer of ^{10}B. Not only did this increase the film adhesion, but it also increased the amount of ^{10}B in the semiconductor which increased the probability of interaction. The new etched approach, seen in Fig. 20, increased the neutron efficiency to 13%.[38]

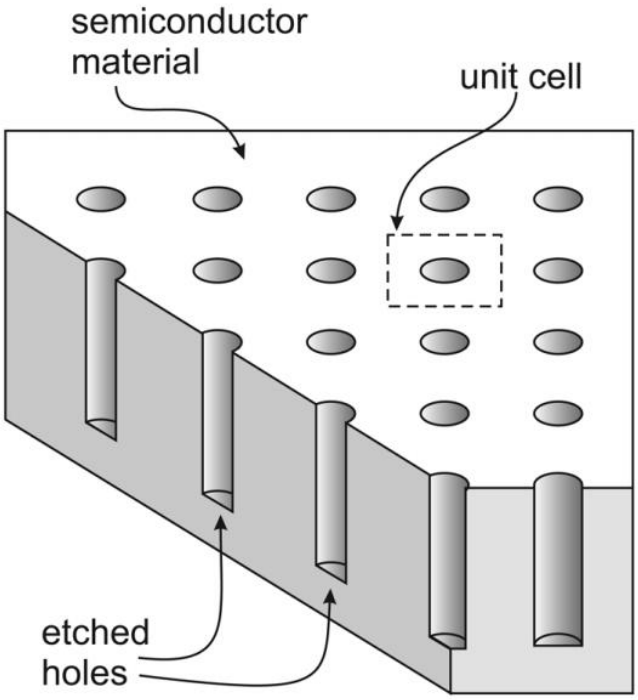

Fig. 20. Conceptual illustration of the basic circular hole design. The holes shown are subsequently shown with neutron reactive ^{10}B.

Although the neutron detection efficiency has been increased due to etching, the amount of energy the reactant particles can impart in the semiconductor decreases, thus decreasing the detectors overall energy resolution. A cross-sectional image of several neutron interaction locations inside the etched semiconductor well loaded with ^{10}B can be seen in Fig. 21., where the cap depth in Fig. 21 is the thickness of the ^{10}B layer imparted on the semiconductor.

In reactions 3,4, and 6 of Fig. 21 above only half of the reactant particles have a path through the semiconductor detector. Since one, or both, of the reactant particles are not detected, the neutron direction vector reconstruction techniques outlined in Sec. III. D. 2 can no longer be applied.

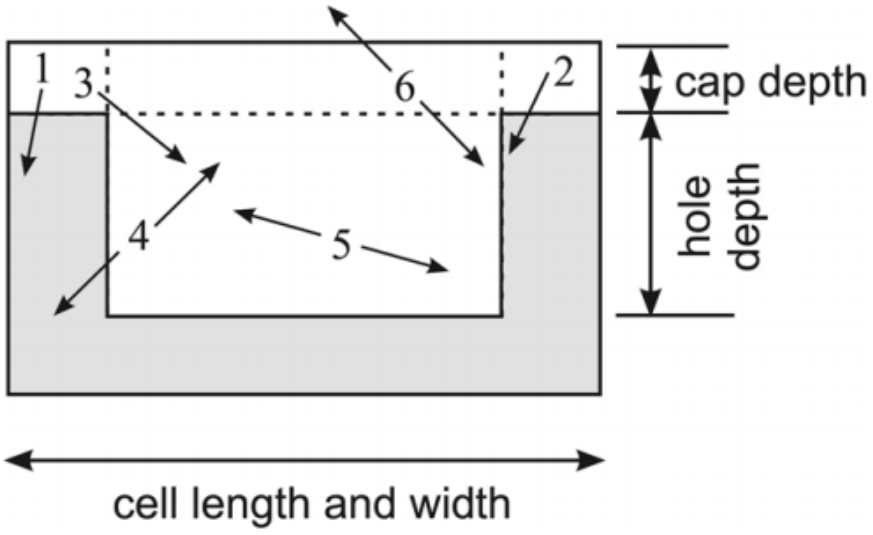

Fig. 21. Cross-sectional view of neutron interaction locations inside an etched semiconductor well loaded with ^{10}B.

In order to receive the full energy deposition for both heavy charged reactant particles in the $^{10}B(n,\alpha)$ reaction, the ^{10}B must be embedded completely in the material. One such material which has ^{10}B in it and is already used in nuclear reactors is B_4C. Although B_4C is one of the strongest materials known to man[39], its low electric conductivity makes it a poor choice to use as a detector medium. If scientific methods find a way to improve the conductivity of B_4C without losing its boron concentration, a prototypical slab type detector would be ideal. This prototype B_4C detector would consists of a series of rotating slab detectors on either side of the vehicle crossing checkpoint. These detectors would hypothetically be robust, and have a large enough detector efficiency and resolution to replicate the incoming neutron direction vector via methods discussed in Sec. III.D.2.

CHAPTER VI

MCNPX SIMULATIONS AND DOPPLER BROADENING CODE DEVELOPMENT

VI.A. Baseline Modeling of Existing RPMs in MCNPX

The first step when creating any new detector configuration is to benchmark an existing detector configuration for comparison. Therefore, a baseline model of the existing RPM at vehicle crossing checkpoints was created in MCNPX. In Sec. II.A.2 a smuggling scenario was referenced in which a shielded HEU source was placed in a briefcase and passed safely through a pedestrian checkpoint containing an RPM. The goal of this section is to recreate a simulation containing a vehicular version of this same smuggling scenario, and observe the RPMs ability to detect the HEU.

Initially, a replica of the RPM discussed in Sec. II.A.1 was recreated in MCNPX. Six ^{3}He cylindrical tubes 6.6 cm in diameter and 89 cm tall were modeled. These ^{3}He tubes were embedded in 2.54 cm of polyethylene for neutron moderation purposes. In front of the ^{3}He tubes, relative to the vehicles position, two PVT scintillators were placed side by side with dimensions 39 cm x 4 cm x 90.75 cm. A cross sectional representation of the modeled RPM detector can be seen in Fig. 22.

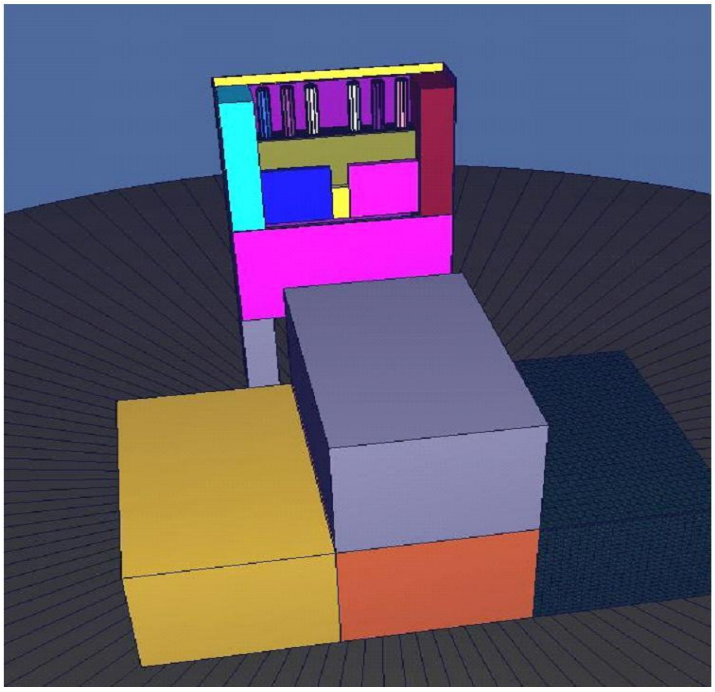

Fig. 22. Illustrated model of the MCNPX created RPM, and adjacent vehicle with HEU in its trunk. The six cylinders in the RPM are the ^{3}He tubes, and the flat blue and pink plates in front of the ^{3}He tubes are the PVT detectors.

The four piece object located in front of the RPM in Fig. 22 is a simplistic design for a motor vehicle. The front compartment (colored yellow in Fig. 22) represents the engine block and is composed entirely of steel. The adjacent two blocks (colored orange and light blue in Fig. 22) represent the passenger compartments comprised of air surrounded by a thin wall of steel. The rear compartment (colored navy blue in Fig. 22) is also a thin steel walled segment representing the vehicles trunk. The lower half of the trunk contains the chemical composition of gasoline, and the upper half contains a 70 at% enriched HEU sphere (500g of U) shielded in concentric spheres of polyethylene and lead. The detector and the vehicle are sitting on top of an earthlike material composed of light metals, carbon and oxygen. Above the ground the detector and the vehicle are surrounded by air composed of nitrogen, carbon, and oxygen. MCNPX will perform a simulation of this vehicle in the location illustrated in Fig. 22, observing the number of ^{3}He(n,p) reactions that occur. Two neutron based simulations

will be performed, the first involves using the shielded HEU as a source emitting neutrons at a rate defined by the source properties, in this case 500 g of 70at% enriched HEU providing 2.144 neutrons per second, with an energy distribution equal to the Watt's spontaneous fission spectrum for ^{240}Pu. The Watt's fission spectrum for ^{240}Pu was chosen because the spontaneous fission spectrum of ^{238}U is not included in the MCNPX library, and the two energy spectrums are nearly identical. The second neutron source was background cosmic neutrons emitted randomly from the air surrounding the vehicle and detector.

VI.B. BF^3 Cloud Chamber Modeling in MCNPX and Doppler Broadening Algorithm Creation

The next step of this research was to model the prototype BF^3 cloud chamber described in Sec. IV.A in MCNPX. Since simulations on BF^3 gas have been previously researched and its efficiency described in Sec.IV.A, the goal in modeling a BF3 cloud chamber detector was to acquire reactant particle information for the creation of a Doppler broadening algorithm.

A cylindrical canister of BF^3 gas, 2 m in diameter by 1 m in height centered at the origin, was modeled in MCNPX. The boron in the BF^3 gas was enriched to 90wt% ^{10}B, and held at 1 atm with a gas density of 0.00276 g/cm3. The BF^3 canister was then surrounded completely by a cylindrical shell of 32Ge 5 cm thick. A model of the BF^3 canister and surrounding ^{32}Ge shell, with the top ^{32}Ge portion removed, can be seen in Fig. 23. The three red spheres in Fig. 23 represent possible source locations for the simulation.

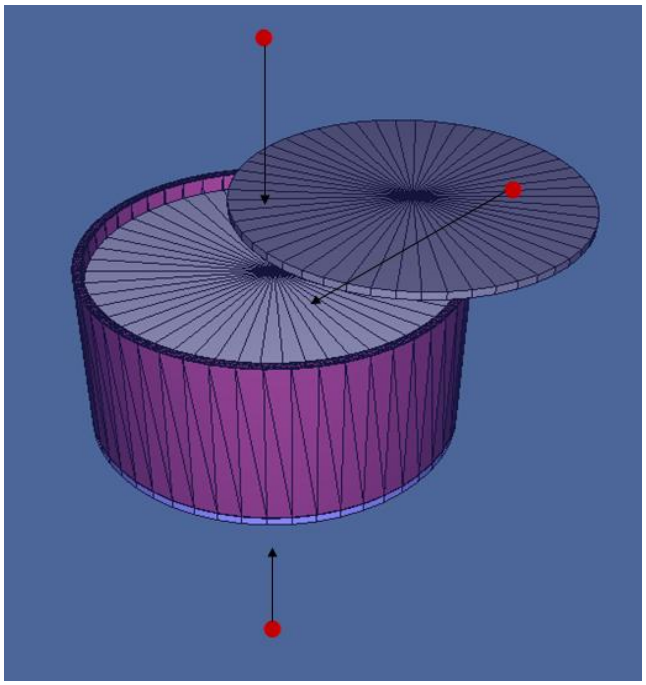

Fig. 23. MCNPX model of a BF_3 prototype cloud chamber surrounded by ^{32}Ge. The three red spheres represent possible neutron source locations.

The source position decided upon was the top red sphere seen in Fig. 23, located 2 m above the center of the BF_3 cloud chamber. Two separate simulations were performed using thermal and 1 MeV neutrons with a collimated neutron source direction vector emitting neutrons in the direction (0,0,-1).

The interaction information from the MCNPX simulations which included particle energies, directions, and reaction types, were listed in an output file using MCNPXs PTRAC feature. A script was then created using the C programming language to filter through the PTRAC output file to extract and store particle interaction information for every excited state $^{10}B(n,\alpha)$ reaction that occurred. The C script would then use this interaction information and the mathematics described in Sec. III.B to Doppler broaden the de-excitation gamma-rays from the simulation. A spectrum of these simulated de-excitation photons were then compared to the analytic and experimental Doppler broadened photons seen in Fig. 11.

VI.C. Initial MCNPX Boron Semiconductor Loading and Efficiency Simulations

Before a prototype RPM using a boron loaded semiconductor can be simulated, a better understanding of the detection properties of boron loaded inside of a semiconductor detector was required. To do this, simulations were performed in MCNPX to find thresholds for detector efficiency by varying boron enrichment and boron semiconductor thickness.

To determine the threshold for detector efficiency with respect to boron enrichment, a borated-silicon detector was modeled in MCNPX. The simulation geometry consisted of a 5 mm borated-silicon wafer with a density of 2.34 g/cm^3 containing 0.01wt% ^{10}B. The borated-silicon wafer was sandwiched between 2, 1 mm thick, pure ^{14}Si wafers with a density of 2.33g/cm^3. A plate approach for the simulation geometry was selected to mimic the boron loaded semiconductors discussed in Sec. IV.B. A collimated thermal neutron source emitting neutrons at 2.144 neutrons per second was then impinged on the center of the sandwiched detector configuration, and the ^{10}B(n,α) reaction efficiency was calculated. The simulation was then repeated increasing the ^{10}B enrichment to values of 0.1 wt%, 0.5 wt%, 1 wt%, 5 wt%, and 10 wt%, and respective ^{10}B(n,α) reaction efficiencies were calculated.

The simulation to determine a threshold for a boron loaded semiconductor plate thickness more closely resembled the detector configuration discussed in Sec. IV.B. In this scenario the vehicle and shielded HEU models from Sec. V.A were replicated. However, the RPM detector configuration in Sec. V.A was replaced by a homogenized plate of B_4C and ^{14}Si isotopically consisting of 17.3 wt% ^{10}B, 2 wt% ^{11}B, 5.7 wt% ^{12}C, and 75 wt% ^{14}Si. The homogenized plate had dimensions of 1 m wide x 3 cm thick x 1.45 m tall and a density of 2.34 g/cm^3. The plate detector configuration is illustrated in Fig. 24 below.

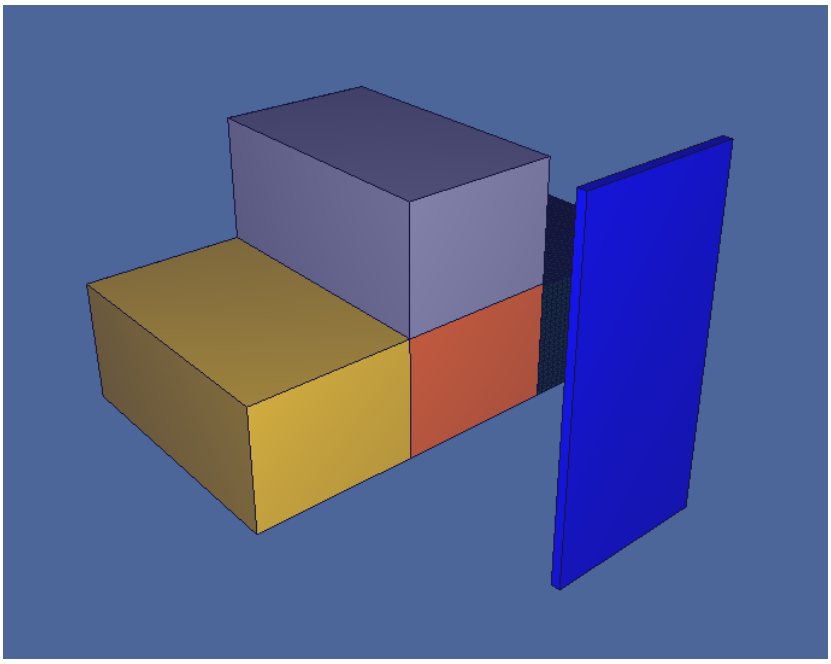

Fig. 24. Model of the vehicle and B_4C plate detector used in MCNPX

The shielded HEU source from Sec. V.A was used with the neutron source strength of 2.144 neutrons per second, and the same ^{240}Pu Watt's fission spectrum energy distribution. A tally for total neutron reactions in the B_4C homogenized plate were recorded, and a $^{10}B(n,\alpha)$ reaction efficiency was calculated. This simulation was then replicated, increasing the plate thickness in increments of 2cm from 5 cm to 35 cm, and respective $^{10}B(n,\alpha)$ reaction efficiencies were calculated.

VI.D. B_4C Detector Simulations

After an acceptable ^{10}B enrichment and B_4C thickness were selected, simulations for a prototype B_4C semiconductor detector were created. The detector configuration chosen was a half cylindrical shell of B_4C divided into four separate, symmetric, pieces. One set of the half cylindrical shell configuration was placed on either side of the simulated vehicle lane. The diameter of both shells was 2 m, and the height of both shells was 1.7 m. The modeled vehicle and HEU shielded from previous sections were again used, and various simulations were performed with the vehicle approaching the

detectors, passing between the detectors, and moving away from the detectors. The purpose of simulating the vehicle at separate points was to imitate the lifelike scenario of a vehicle passing through a vehicle monitoring station. A representation of the detector configuration with the modeled vehicle can be seen in Fig. 25.

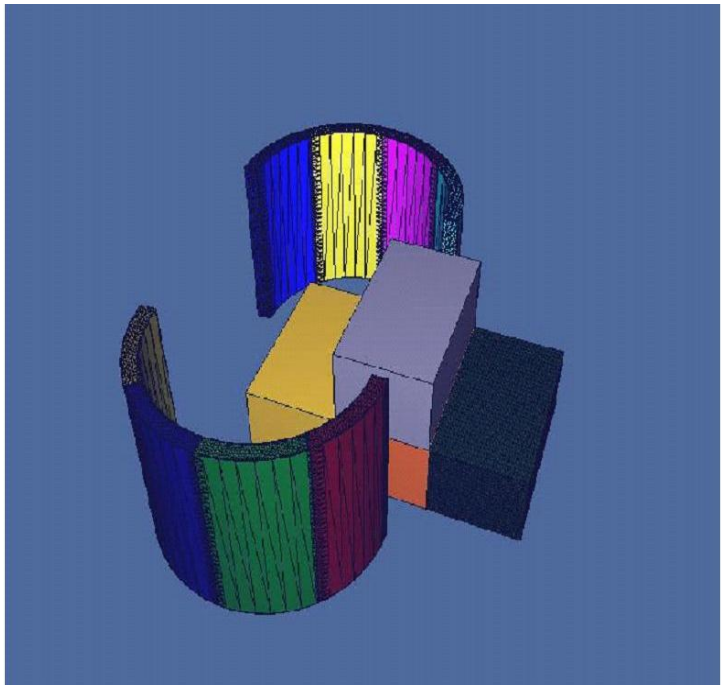

Fig. 25. B4C detector half cylinder detector configuration with a model vehicle between the two detectors.

CHAPTER VII

RESULTS AND SENSITIVITY ANALYSIS

VII.A. Baseline RPM Results

As mentioned in Sec. V.A, the purpose of simulating the existing RPM detector configuration was to determine its capability to detect shielded HEU in a smuggling scenario. The results from the HEU and background source simulations in MCNPX can be seen in Table 4.

Table 4.

RPM Baseline Simulation Results.

Configuration	3He(n,p) Reactions per second
HEU Source Only	1.40E-04
Background Only	2.51E-01

When looking at Table 4 there are two elements that incite concern. The first is the exceedingly low ^{3}He(n,p) reaction rate inside the ^{3}He neutron detectors. A count rate on the order of 1E-4 counts per second would require the count time of the vehicle to be exceedingly long to achieve sufficient statistics. As an example, these results illustrate that if a vehicle containing a shielded HEU source were parked in front of an RPM detector configuration for an hour, less than one neutron would be detected in the ^{3}He tubes from the HEU source. The second troubling element to be noted is the relationship between the source strength and background strength. Not only would an excessive count time be required for a shielded HEU source, the counts received from background alone would make the very few counts received from the HEU source become indistinguishable. Due to the concerning results from this model, it is verified with a resounding certainty that the existing RPMs at vehicle crossing checkpoints are incapable of distinguishing neutrons from a shielded HEU source. Therefore, the research to upgrade the existing RPMs at vehicle crossing checkpoints is warranted.

VII.B. BF_3 Cloud Chamber Simulation and Doppler Broadening Algorithm Results

The primary goal of the BF_3 cloud chamber simulations was to verify that MCNPX could accurately handle the Doppler broadening of de-excitation photons from the $^{10}B(n,\alpha)$ reaction. After the BF_3 cloud chamber was modeled in MCNPX and a few baseline simulations were performed, it was confirmed that MCNPX was in fact, not applying the correct Doppler broadening mathematics to the de-excitation gamma-rays. MCNPXs PTRAC function was used to list parameters for every particle interaction that occurred. The simulation variables that are listed by PTRAC include particle location, energy, direction, reaction type, and the time the reaction occurred. After looking at the first few listed de-excitation gamma-ray reactions, it quickly became evident that there was not a conservation of energy between reactant particles and the incoming neutron via the manner described in Sec. III.B. A conservation was not applied to reactant particles because of the way the random MC method operates. MCNPX simulates the complete neutron lifetime first, including the locations of every interaction site, and then samples the types of interactions that occur at said interaction sites using reaction probabilities. Therefore, when MCNPX decides that a $^{10}B(n,\alpha)$ reaction occurs, a random distribution of directions are given to the reactant $^{7}Li^{*}$ and ^{4}He particles instead of the required distributions that obey the conservation principles outlined in Equations 3-10. Since the particle information listed by PTRAC did not obey the appropriate conservation equations, the Doppler broadening of the de-excitation gamma-ray could not be calculated.

To correctly Doppler broaden the MNCPX simulated de-excitation gamma-rays, the Doppler broadening algorithm mentioned in Section V.B was created. The algorithm used the mathematics described in Equation 11 in conjunction with the PTRAC listed energy and direction of the $^{7}Li^{*}$ particle, and a randomly generated angle for the de-excitation gamma-ray sampled from 4π distribution to produce the results seen in Fig. 26.

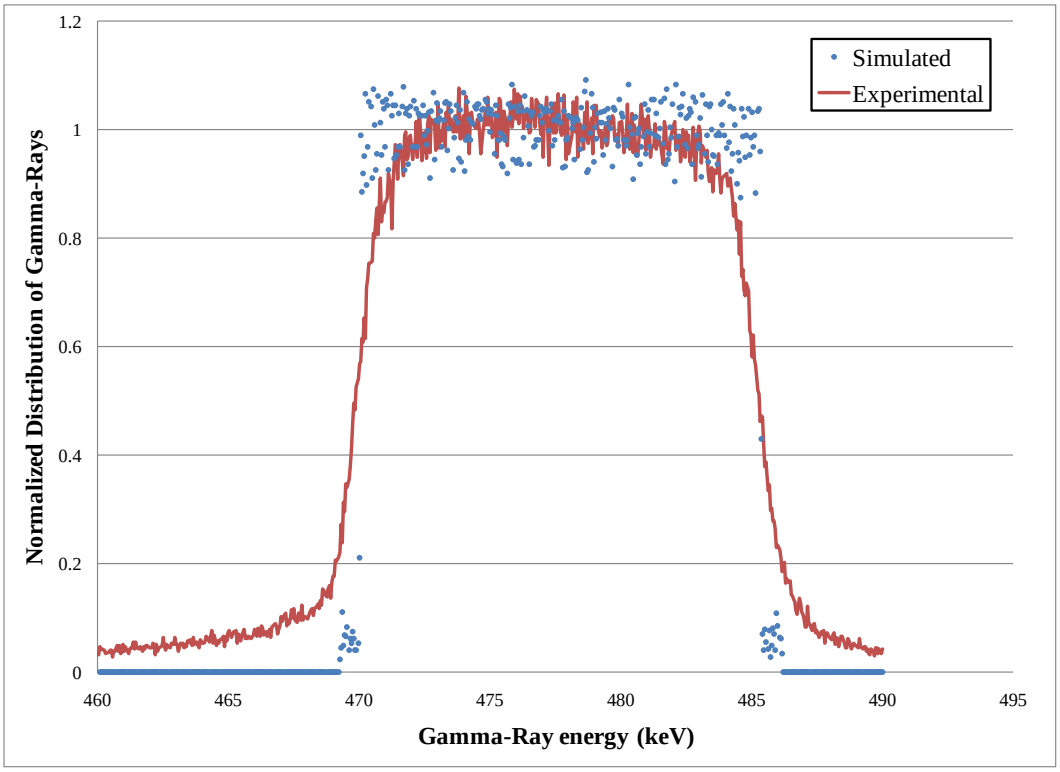

Fig. 26. MCNPX Doppler broadened gamma-rays versus experimentally Doppler broadened gamma-rays created from the thermal neutron reaction $^{10}B(n,\alpha)$.

As is seen in Fig. 26, the MCNPX spectrum matches up very well with the experimental Doppler broadened spectrum. The slight difference between the two spectra reside in the edges of the Doppler broadened "hump" in the simulated data, which can be attributed to the exclusion of detector resolution in the simulation similar to Fig. 11. The difference between the MCNPX spectrum and the experimental spectrum for energies greater than 486 keV can be attributed to background noise in the experimental system. Likewise, for energies below 470 keV the difference between the spectrums can be attributed to background noise, as well as additional counts from the Compton distribution for gamma-rays in the de-excitation "hump". Due to the similarity between the spectrums presented in Fig.26, the accuracy and validation of the de-excitation Doppler broadening algorithm created in the C programming language is confirmed.

VII.C. B_4C Simulation Results

VII.C.1. Boron Enrichment and B_4C Thickness Simulations

Before a prototype B_4C vehicle monitoring detector could be modeled in MCNPX, a set of primary simulations were required to determine basic detector parameters such as boron enrichment and semiconductor plate thickness. In order to determine the ideal enrichment of ^{10}B in a boron loaded semiconductor, several MCNPX simulations were performed on a slab of borated silicon with varying ^{10}B enrichments. The borated silicon was sandwiched between two thin sheets of ^{14}Si to more closely resemble detector configurations discussed in Sec. IV.B. The results from these simulations are shown in Fig. 27.

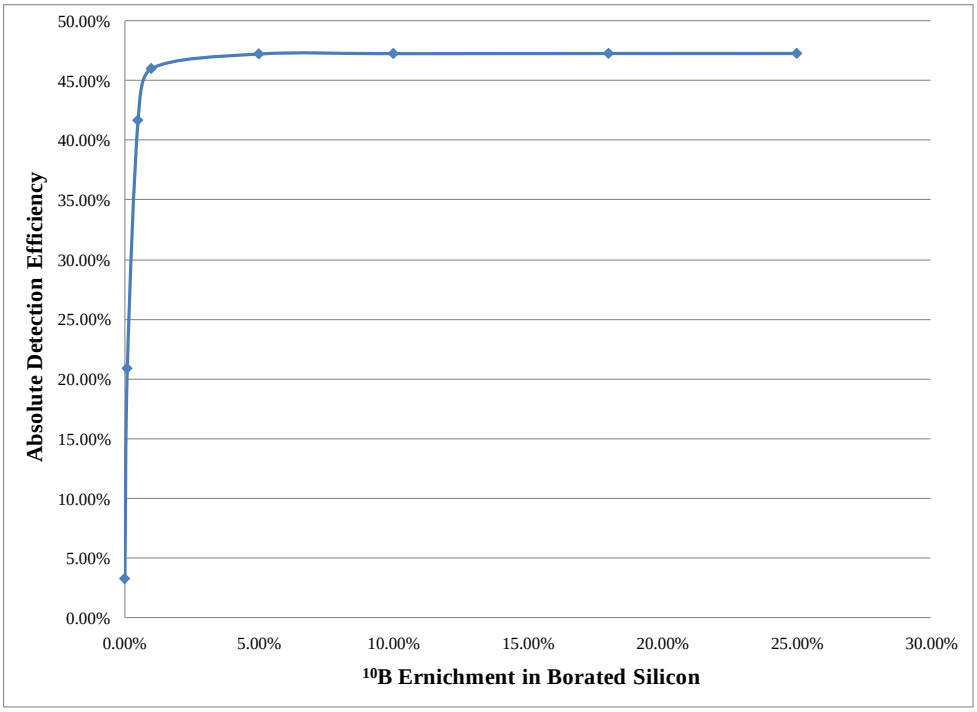

Fig. 27. Simulation results for ^{10}B enrichment in a borated silicon wafer.

The results from the ^{10}B enrichment simulations are successful at giving information about two key detector characteristics in boron loaded semiconductors. The first is that small levels of boron enrichment are capable of producing the same detector efficiency as larger enrichments as seen in Fig. 27. Therefore, due to the amount of ^{10}B

in commercially available B_4C, which is approximately 75 wt%, further enrichment of ^{10}B in later simulated B_4C is not necessary. Results from Fig. 27 also provide information about the necessary size of the detector. The capability of the 5 mm thick borated silicon detector configuration to capture nearly half of the 2.144 thermal neutrons emitted per second is promising. These capture efficiency results lend credence to the idea that an increased detector thickness can increase the overall detection efficiency in the system.

To determine B_4C thickness characteristics in a vehicle monitoring scenario, simulations were performed varying plate thicknesses of B_4C with the same shielded HEU neutron source used in the benchmark simulations. The results from these simulations are depicted in Fig. 28.

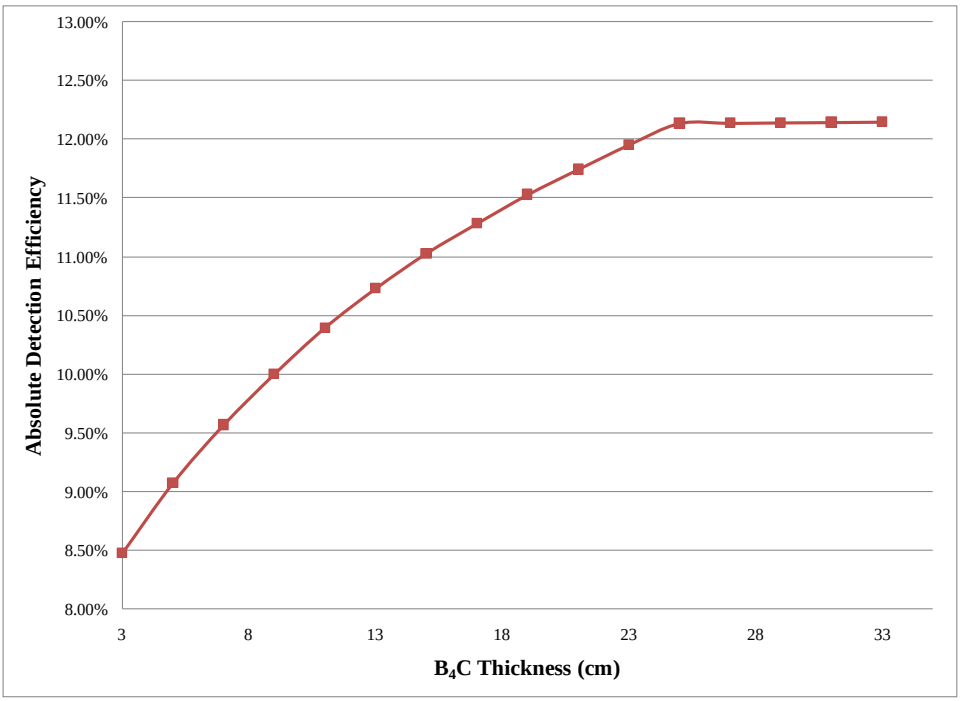

Fig. 28. Detection efficiency versus B_4C thickness.

The first major discrepancy between the results displayed in Fig. 27 and Fig. 28 is the drop in absolute detection efficiency. This drop in detection efficiency is attributed to the difference in energy spectrums for each simulation. The results of Fig. 27 are

based on a thermal neutron energy spectrum used specifically to determine the effect of modifying ^{10}B enrichment. Conversely, the results of Fig. 28 use a higher energy, ^{240}Pu Watt's spontaneous fission spectrum, in order to mimic vehicle monitoring station scenarios. Since the increase in detection efficiency plateaus at a B_4C thickness of 25 cm, the thickness of all B_4C semiconductor detectors simulated after this was 25 cm. It is important to mention that although an absolute detection efficiency of 12% seems low compared to the thermal neutron simulation of Fig. 27, the detection efficiency of the large B_4C plate detectors seen in Fig.28 is nearly 100 times greater than those seen in Fig. 19 using a ^{252}Cf source and BF_3 tubes.

VII.C.2. B_4C Prototype Vehicle Monitor Results

After the ^{10}B enrichment and B_4C plate thickness was selected, the remaining element before creating a prototype B_4C vehicle monitor was to decide upon a geometric configuration. Since a crucial element of almost every safety system or detection configuration involves redundancy, the goal was to create a geometric B_4C configuration such that it had redundant directionality capabilities. Along with the material properties of B_4C that enable it to reconstruct an incoming neutrons direction vector, a geometric detector configuration was designed that would use raw count data to provide directional information about the source location. The system conceived was a pair of 25 cm thick half cylindrical shell detectors described in Sec. V.D. The results of the moving vehicle simulations using half cylindrical shell detectors can be seen in Fig. 29. A revised version of Fig. 25 displaying detector quadrant numbers can be seen in Fig. 30.

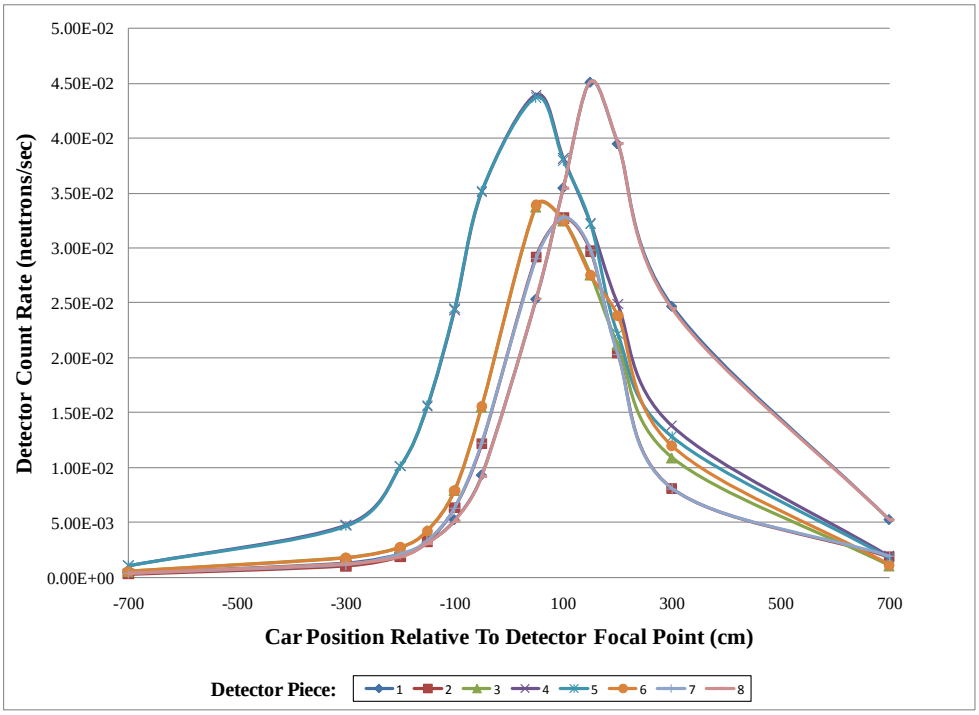

Fig. 29. Simulation results for a mock vehicle passing through two half cylindrical B_4C detectors. Each B_4C detector was divided into quadrants leaving eight total detector pieces to accumulate count data.

By simply observing the shape of the count information received by separate detector pieces seen in Fig. 29, the location of the incoming HEU source can be inferred. Since detector pieces 1 and 8 have the greatest solid angle relative to the approaching vehicle, the shape of the function of their counts maximizes after the trunk of the vehicle passes through the center of the detector. Similarly, the shape of the counts function for detector pieces 4 and 8 maximize shortly after the entire vehicle passes through the detector configuration. This is again due to the large solid angle that these detector pieces posses for a vehicle traveling away from the detector configuration. If the count information for every detector piece were summed, the maximum of the count shape function would occur when the HEU source passes through the center of the half cylinder detectors.

Since the HEU source is located in the trunk of the vehicle, the expected crest of the summed count function should occur as the vehicle is slightly past the focal point of the half cylinder detector. This is precisely the case, as seen in Fig. 29, thus the ability for the half cylindrical detector configurations to geometrically provide directionality information is verified.

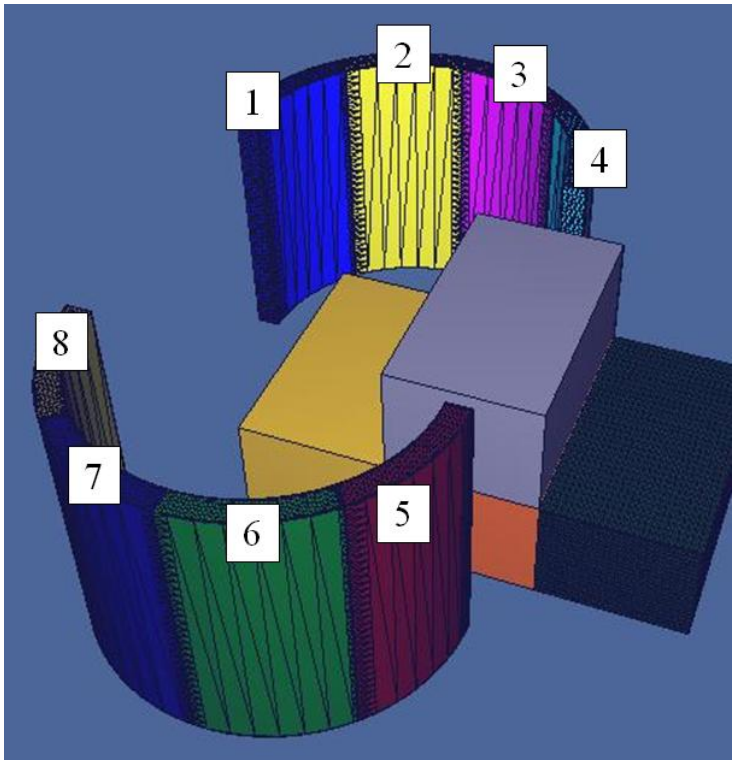

Fig. 30. Half cylindrical B_4C detector configuration with numbered detector quadrants. In the moving vehicle simulation the vehicle travels from left to right relative to this depicted configuration. The HEU source is in the trunk of the vehicle.

It is also important to note that due to the size of these detector configurations, the overall count rate in the prototype vehicle monitor is increased by a factor of nearly 100 when compared to the existing RPM detectors. An example of this can be seen by comparing the benchmark RPM count rate information received from the source only simulation in Table 4, with the count rate information of the half cylindrical B_4C

detectors seen in Fig. 29. Both of these simulations used a neutron source with identical emission rates and energy spectrums.

VII.D. Inverse Analysis Results

With the verification of the Doppler broadening algorithm and two prototype detector configurations successfully simulated, the next step was to recreate the incoming neutron direction vector for both prototype detector simulations using the methods described in Sec. III.D.

VII.D.1. Recreating BF_3 Cloud Chamber Incoming Neutron Vectors

As described in Sec. III.D.1., recreating neutron direction vectors from cloud chamber detector data is simply a matter of applying conservation principles. Using Equations 13-15 in conjunction with the manufactured α information from Equations 16-18, Equations 13-15 can be used to calculate the incoming neutron direction vectors for the simulation described in Sec. V.B. Some of the recalculated neutron information from the BF_3 prototype detector simulation can be seen in Table 5.

Since the recreated neutron direction cosines are calculated using manufactured solutions of α particles, and the manufactured solutions for α are created from a modified version of the same equations, the difference between the two simulated and recreated directions should be attributed only to round off error. In Table 5, the recreated neutron direction cosines calculated were so precise that there was not a difference between the calculated and simulated neutron direction information.

Table 5.

MCNPX Neutron Information Versus Recreated Neutron Information.

MCNPX Neutron Direction Cosine					**Recreated Neutron Direction Cosine**				Δθ
Particle #	u_n	v_n	w_n	$\theta_{n\cdot li}$ (°)	u_n	v_n	w_n	$\theta_{n\cdot li}$ (°)	
7	0	0	-1	97.70	0	0	-1	97.70	0
223	-0.7802	0.35724	-0.5135	110.84	-0.7802	0.35724	-0.5135	110.84	0
248	0.0914	-0.7264	-0.6812	157.96	0.0914	-0.7264	-0.6812	157.96	0
309	0	0	-1	63.98	0	0	-1	63.98	0
375	-0.4795	-0.4304	-0.7648	97.42	-0.4795	-0.4304	-0.7648	97.42	0
691	0.0381	0.21698	-0.9754	59.92	0.0381	0.21698	-0.9754	59.92	0
868	0	0	-1	52.02	0	0	-1	52.02	0
900	-0.5465	-0.3798	-0.7464	41.36	-0.5465	-0.3798	-0.7464	41.36	0
904	0.68442	0.56711	-0.4582	123.47	0.68442	0.56711	-0.4582	123.47	0

Δθ: The difference in angle in degrees between the MCNPX direction vector, and the recalculated neutron direction vector.

VII.D.2. Recreating B_4C Semiconductor Incoming Neutron Vectors

To recreate incoming neutron direction information from B_4C semiconductor detectors, a directional triangulation from multiple incoming neutron cone surface solution sets is required. The neutron cone surface solution sets are created using de-excitation gamma-ray information in conjunction with the method of superposition of cones discussed in Chapter IV to create a neutron cone surface, numerical methods are used to calculate and iterate upon possible $^{7}Li^{*}$ and neutron direction cosines that validate Equation 21. Since iterative methods are not discussed in this research, the recreated incoming neutron direction vector can be validated by verifying that the calculated and simulated variables that make Equation 21 equal to zero. These variables as well as the method by which they were obtained are outlined in Table 6.

Table 6.

Variable Information Used in Equation 21 to Calculate a Neutron Cone Surface.

Particle	U	V	W	Numerical Iteration	MCNPX Data	Calculated Data
n	-0.1455	-0.4122	0.3027	**X**		
$^{7}Li^{*}$	-0.2737	-0.7753	0.5693	**X**		
γ^{*}	-0.5898	0.7672	-0.2521		**X**	
$\theta_{\gamma^{*}\cdot Li}$ (degrees)	54.77					**X**
$\theta_{n\cdot Li}$ (degrees)	112.17					**X**

The variable information from Table 7 is then inserted into Equation 21 to determine if the neutron direction vector created from the numerical simulation lies on the neutron cone surface. If the incoming neutron direction vector does lie on the cone surface, S(u) should equal zero. The particle information from Table 6 applied to Equation 21 can be seen in Table 7.

Table 7.

Evaluation of Variables from Table 6 in Equation 21.

	Degrees
$(u,v,w)_{\gamma^{*}} \cdot (u,v,w)_{Li}$	54.77
$(u,v,w)_{n} \cdot (u,v,w)_{Li}$	110.84
$\theta_{\gamma^{*}\cdot Li}$	54.77
$\theta_{n\cdot Li}$	112.17
S (u)	1.33

The difference in the value for the solution of Equation 21 seen in Table 7, and the expected value of zero can be attributed to mathematical round off error from Equations13-15. Although the evaluation data of Table 7 does not exactly equal zero, the error is small enough to accurately presume the neutron direction vector used to attain these results lies on the surface of the neutron cone. If multiple $^{10}B(n,\alpha)$ interactions

occurred in the same region, a triangulation of neutron surface cones would give the incoming neutron direction vector for the neutron source.

VII.E. Sensitivity Analysis Results

The methods of Chapter IV have outlined the process for recreating the incoming neutron's direction vector in two detector configurations. It is now important to understand the sensitivity these processes have to small perturbations in detected data. In order to equally compare the sensitivity in both detector configurations, "deviation" coefficients were created based off of each detector's capabilities. Since the detectors response to the accuracy with which it records energy and angle information is vital to recreating the incoming neutron direction vector, detector energy and angle resolution were chosen as these coefficients. For the cloud chamber, energy and angular resolutions of 5 KeV and 0.2° were used. For the semiconductor detector, energy and angular resolutions of 10 KeV and 0.5° were used. To test the sensitivity of the neutron direction vector recreation process, the data received by the detector was perturbed by units of detector resolution, or "deviations", and the affects were observed. After the incoming neutron direction vectors have been calculated for both prototype detector configurations, a representation of the sensitivity to detector accuracy was desired. In order to determine this sensitivity, the MCNPX simulation data was altered by a sensitivity coefficient and the results were observed.

VII.E.1. Sensitivity Analysis for the BF_3 Cloud Chamber

The sensitivity of the calculated incoming neutron direction to a series of perturbations on the $^{7}Li^{*}$ energy and direction information received from MCNPX was determined. These results are displayed in Table 8.

Table 8.

Sensitivity Results for Perturbations of the $^{7}Li^{*}$ Particle Direction Vector in the Prototype BF_3 Cloud Chamber Detector.

# Of Deviations	Induced Perterbation (degrees)	Difference Between Calculated and MCNPX Neutron Vector (degrees)	Sensitivity Coefficient
0	0.0000	0.8102	----
1	0.1971	1.0124	5.1358
2	0.4075	1.3001	3.1905
3	0.6186	1.6365	2.6455
4	0.8323	2.0044	2.4083
5	1.0490	2.3957	2.2838

Observing the results from Table 8, the difference between the calculated neutron direction vector, and the MCNPX produced neutron vector is less than three degrees at five sensitivity deviations. The discrepancy between the calculated and simulated neutron direction vectors at zero perturbations can be attributed to round off error in the mathematics. The sensitivity coefficient, which is defined as a ratio of the induced $^{7}Li^{*}$ angular perturbations to the difference between simulated and calculated neutron vectors, is a good quantification for the relationship between the number of deviations and the difference in the calculated neutron vector. As indicated by Table 8, the difference in neutron vectors is most sensitive to the first sensitivity deviation, and then decreases with every following sensitivity deviation. The results for perturbing both angle and energy information is seen in Table 9.

Table 9.

Sensitivity Results for Perturbations of the $^{7}Li^{*}$ Particle Energy and Direction Vector in the Prototype BF_3 Cloud Chamber Detector.

# Of Deviations	Induced Angular Perterbation (degrees)	Induced Energy Perterbation (MeV)	Difference Between Calculated and MCNPX Neutron Vector (degrees)	Sensitivity Coefficient
0	0.0000	0.0000	0.8102	----
1	0.1971	0.0050	1.1643	5.9062
2	0.4075	0.0100	1.5167	3.7221
3	0.6186	0.0150	1.8663	3.0169
4	0.8323	0.0200	2.2126	2.6584
5	1.0490	0.0250	2.5555	2.4361

The results of Table 9 conclude that perturbing both angle and energy in the system slightly increase the difference in angle between the calculated and simulated neutron vector. The increase is nearly negligible however, and it is still important to note that the difference in angle at five sensitivity perturbations is less than three degrees.

VII.E.2. Sensitivity Analysis for the B_4C Semiconductor Detector

A sensitivity analysis was also performed for the prototype B_4C semiconductor detector. Similar to the previous section, an analysis on the effect of perturbing the $^{7}Li^{*}$ direction vector alone is compared with perturbing both the direction vector and energy of the $^{7}Li^{*}$ particle. Results from the direction vector only perturbation can be seen in Table 10.

Table 10.

Sensitivity Results for Perturbations of the $^{7}Li^{*}$ Particle Direction Vector in the Prototype B_4C Semiconductor Detector.

# Of Deviations	Induced Perterbation (degrees)	Difference Between Calculated and MCNPX Neutron Vector (degrees)	Sensitivity Coefficient
0	0.0000	1.3296	----
1	0.5002	1.9268	3.8518
2	0.9941	2.5118	2.5268
3	1.4769	3.0848	2.0888
4	1.9495	3.6461	1.8703
5	2.4123	4.1959	1.7394

The results from Table 10 show a larger difference between the calculated and simulated neutron direction vector as well as a lower sensitivity coefficient. At five sensitivity perturbations, the difference between the two direction vectors is almost double the values seen in a cloud chamber detector. The larger difference in calculated angle can be attributed to lower semiconductor angular resolution and mathematic round off error. Because a semiconductor detector has a lower angular resolution relative to a cloud chamber, the deviation coefficient increases. With a larger deviation coefficient, the induced perturbation per deviation increases, thus increasing the difference between the calculated and simulated neutron direction vector relative to a cloud chamber.

The increase in deviation coefficient also plays a factor in the decrease of the sensitivity coefficient. Due to the definition of the sensitivity coefficient, having a larger deviation coefficient increases the denominator of the coefficient, thus decreasing its overall value. It is also important to note that due to the mathematics behind direction vector reconstruction in semiconductor detectors, the angular difference attributed to round off error is also greater than that of a cloud chamber detector. The results from perturbing both the energy and direction vector of the $^{7}Li^{*}$ reactant particle in a semiconductor detector can be seen in Table 11.

Table 11.

Sensitivity Results for Perturbations of the $^{7}Li^{*}$ Particle Energy and Direction Vector in the Prototype B_4C Semiconductor Detector.

# Of Deviations	Induced Angular Perterbation (degrees)	Induced Energy Perterbation (MeV)	Difference Between Calculated and MCNPX Neutron Vector (degrees)	Sensitivity Coefficient
0	0.0000	0.0000	1.3296	----
1	0.5002	0.0100	2.9030	5.8032
2	0.9941	0.0200	4.4828	4.5094
3	1.4769	0.0300	6.0701	4.1101
4	1.9495	0.0400	7.6664	3.9326
5	2.4123	0.0500	9.2732	3.8441

Similar to results from Table 9, the difference between simulated and calculated neutron vectors increase when both energy and direction are perturbed. At five sensitivity deviations, the difference in direction vector for a semiconductor is roughly five times what it is in a cloud chamber detector. The difference in the calculated angle is larger in a semiconductor detector because of the increased deviation coefficient and a lack of information about reactant particles. Since only the energy of the reactant particles are known in a semiconductor detector, the process of manufacturing the reactant particles angular information introduces additional error into the system. It is important to note that if these results were treated as a Gaussian distribution, where there would be greater than a 99.6% probability the solution would lie within three deviations, an error of six degrees for the incoming neutron vector is more than acceptable.

CHAPTER VIII

FINALIZED DETECTOR DESIGN

It has been shown in this research that there are many advantages to using a semiconductor detector configuration. Therefore, a combination of B_4C and ^{14}Si will be used for the newly proposed RPM detector configuration. Due to the results from simulated detector enrichment calculations, the standard enrichment of 75wt%^{10}B in B_4C is acceptable. Using commercially available B4C allows for an economic advantage due to its accessibility from wide use in nuclear reactor configurations.

The new RPM detector will consist of 5 mm thick plates of B_4C sandwiched between 1mm plates of ^{14}Si. In order to reach the nominal B_4C thickness of 25 cm, 250 of these B_4C plate configurations will be stacked together. The stacked plates of B_4C and ^{14}Si will be molded into a half cylindrical shell type detector, similar to the configuration seen in Fig. 25. The detector will stand 1 m tall and have a diameter of 2 meters.

A single half cylindrical B_4C detector divided into quadrants will be placed on either side of the vehicle lane. The focal point of the half cylindrical configuration should be located approximately 1 m from the edge of the lane. A rotatable motor will then be placed underneath the bottom of each detector quadrant to aid in SNM detection in lanes near the detector. The inclusion of rotation capable detector quadrants increases the geometric directional capabilities in the system. By rotating the detector quadrants in adjacent lanes to face one containing SIM, the solid angle for multiple detectors is increased, thus increasing the capability for larger detection efficiency.

CHAPTER IX

SUMMARY AND CONCLUSIONS

The increased probability of nuclear attack and the dated technology with which RPMs are created, inspired research into the field of directionally sensitive neutron detectors. Before new prototype detector configurations could be considered, a series of smuggling simulations were performed in MCNPX on existing RPMS to determine the probability of detection. A shielded 500 g HEU source at 70at% had an active count rate of 1.40E-4 neutrons per second. A count rate as low as this would require the vehicle to remain in front of the detector for over an hour to accumulate the same amount of neutrons detected in one second of background irradiation.

After the fallibilities in existing RPM detector configurations were shown, the methods to creating a direction sensitive neutron detector were discussed. Among these methods, the uniqueness of the Doppler broadened $^{7}Li^{*}$ de-excitation gamma-ray was highlighted. Experimental and analytical results were shown to prove the existence of the Doppler broadened gamma-ray. It was then shown that by using this de-excitation gamma-ray information in conjunction with the other reactant particle information from the $^{10}B(n,\alpha)$ reaction, the incoming neutron direction vector could be reconstructed. Using conservation principles and the method of cone superposition, the mathematics for recreating the incoming neutron direction vector in a boron loaded cloud chamber and boron loaded semiconductor were derived.

Simulations in MCNPX were performed on a cloud chamber loaded with BF_3 to determine if MCNPX could accurately Doppler broaden the $^{7}Li^{*}$ de-excitation gamma-rays. Once it was determined that MCNPX did not Doppler broaden these gamma-rays, a Doppler broadening algorithm was created. The algorithm was created using the C programming language and made use of MCNPXs PTRAC function to manually Doppler broaden de-excitation gamma-ray produced from the simulation. This spectrum of created Doppler broadened de-excitation gamma-rays was then compared to the simulated and analytical spectrums and matched with a high degree of accuracy.

Further simulations were performed in MCNPX to provide detector characteristic information about boron loaded semiconductors. Using the aforementioned 500 g HEU source emitting 2.144 thermal neutrons per second, the detection efficiency for a 5 mm thick ^{10}B doped ^{14}Si plate detector was found to plateau at 50%, with a corresponding ^{10}B enrichment of 3wt%. Another simulation performed in MCNPX found that the ideal plate thickness for a B_4C semiconductor detector at ^{10}B enrichment of 75wt% was 25 cm thick. Further simulations in MCNPX were performed on a half cylindrical shell of B_4C plate detectors to determine the systems geometric directional capability. These simulations not only showed that the detector configuration was capable of locating the direction of a neutron source from raw count information alone, but also the B_4C plate detectors increased the neutron count rate to the order of 2E-02 counts per second.

MCNPX were then performed simulations on both a prototype ^{10}B loaded cloud chamber and prototype ^{10}B loaded semiconductor detector were performed, and incoming neutron direction vectors from each detector configuration were recalculated using the simulated particle reactant data provided by PTRAC. A sensitivity analysis was then performed on each detector configurations ability to accurately reconstruct incoming neutron direction vectors. By modifying the energy and direction vector of the simulated PTRAC output data for $^{7}Li^{*}$ particles, three deviation coefficients showed a respective angular uncertainty of 1.86° and 6.07° for a boron loaded cloud chamber and a boron loaded semiconductor.

Lastly, a new B_4C half cylindrical RPM detector configuration was described. The B4C detector would be 1 m tall x 2 m in diameter x 25 cm thick, with a ^{10}B enrichment of 75wt%. Each half cylindrical detector configuration would be divided into quadrants that could be rotated to maximize geometric detection efficiency.

The robustness and increased detection efficiencies of a B_4C prototype RPM give it an attractive advantage over the dated RPM detectors currently in service. Future work in this area of research should be performed on increasing the neutron angular detection efficiency in semiconductor detectors, as well as improving the directional detection capability of sandwiched ^{14}Si Detectors. Although there are certain technological factors

that prevent a B_4C detector configuration from being created in the present, the ideas and methods presented in this research offer insight into the possibilities of using ^{10}B for neutron direction reconstruction.

REFERENCES

1) "DHS Improved Testing of Advanced Radiation Portal Monitors, but Preliminary Results Show Limits of New Technology", Government Accountability Office (2009), available on the Internet at <*http://www.gao.gov/htext/d09655.html*>
2) "Illicit Nuclear Trafficking in the NIS", S. PARRISH (2002), available on the Internet at <*http://www.nti.org/e_research/e3_8a.html*>
3) V.A. ORLOV, "Illicit Nuclear Trafficking & the New Agenda", *IAEA Bulletin 46/1,* 3 (2004).
4) "Nuclear Black Markets: Pakistan, A.Q. Khan and the Rise of Proliferation Networks", International Institute for Strategic Studies (2007), available on the Internet at <*http://www.iiss.org/publications/strategic-dossiers/nbm/*>
5) L. ZAITSEVA, and K. HAND, "Nuclear Smuggling Chains", *Amer. Behavioral Scientist*, **40.6**, 822 (2003).
6) "International Terrorism and Transnational Crime: Security Threats, U.S. Policy, and Considerations for Congress", Congressional Research Service (2010), available on the Internet at <*http://www.loc.gov/crsinfo/*>
7) "Detecting Nuclear and Radiological Materials", The Royal Society (2008), available on the Internet at <*http://www.royalsociety.org*>
8) J.L. DARBY, "Evaluation of Risk for Acts of Terrorism Using Belief and Fuzzy Sets", *J. Nuclear Materials Management*, **35**, 19 (Winter 2007).
9) "Radiation Portal Monitors", Department of Homeland Security (2002), available on the Internet at <*http://www.dhs.gov/index.shtm*>
10) R.T. KLANN, J. SHERGUR, and G. MATTESICH, "Current State of Commerical Radiation Detection Equipment for Homeland Security Applications", *Nuc. Tech.*, **169**, 79 (Oct. 2009).
11) R.J. HOWERTON, "Thresholds and Q Values of Nuclear Reactions Induced by Neutrons, Protons, Deuterons, Tritons He-3 Ions, Alpha Particles, and Photons." *NASA STI* 24 (1981).

12) "Helium-3 Shortage for Radiation Portal Monitors is Severe, DHS Warns", C. BIESECKER (2006), available on the Internet at *<http://findarticles.com/p/articles/mi_6712/is_33_244/ai_n45231171/?tag=content;col1>*

13) T.B. COCHRAN, and M.G. MCKINZIE, "DETECTING NUCLEAR SMUGGLING.", *Scientific American Military & Govt. Collection*, **298.4**, 98 (2008).

14) L. SWIDERSKI, "Comparison of Neutron Detection Efficiency of a He-3 Counter and a Boron-10 Loaded Liquid Scintillator.", *IEEE Transactions on Nuclear Science*, **57.5**, 2857 (2010).

15) B. AYAZ-MAIRHAFER, and T.A. DEVOL, "Determination of Absolute Detection Efficiencies for Detectors of Interest in Homeland Security", *Nucl. Instr. Meth. in Phys. Res.*, **579**, 410 (2007).

16) K.KODAMA, "Momentum Measurement of Secondary Particle by Multiple Coulomb Scattering with Emulsion Cloud Chamber DONuT Experiment", *Nucl. Instr. Meth. in Phys. Res.*, **574**, 192 (2007)

17) M.F. KAPLON, and D.M. RITSON, "Emulsion Cloud-Chamber Observations on the Interactions of High Energy Primary Cosmic Radiation", *Physical Review*, **88.2**, 386 (Oct. 1952).

18) W.A. NELSON, "Cloud Chamber", *The Hoosier Science Teacher*, **20.1**, 13 (1994).

19) M. DE SORIO, "Momentum Measurement by the Angular Method in the Emulsion Cloud Chamber", *Nucl. Instr. Meth. in Phys. Res.*, **512**, pp. 539-545 (2003).

20) A. ROCCARO, "A Background-free Direction-sensitive Neutron Detector", *Nucl. Instr. Meth. in Phys. Res. A*, **608**, 305 (2009).

21) J.E. TURNER, *Atoms, Radiation, and Radiation Protection*, 2nd Ed., John Wiley & Sons, New York (1995).

22) G.F. KNOLL, *Radiation Detection and Measurement*, 3rd Ed., John Wiley & Sons, New York (2000).

23) G.J. SCHMID, "Gamma-ray Compton Camera Imaging with Segmented HPGE", *Nucl. Instr. Meth. in Phys. Res.*, **459**, 565 (2001).

24) Y.F. YANG, Y. GONO, S. MOTOMURA, S. ENOMOTO, and Y. YANO, "A Compton Camera for Multitracer Imaging", *IEEE Transactions on Nuclear Science*, **48.3**, 656 (June 2001).

25) J.S. BRENIZER, "Development of a New Electronic Neutron Imaging System", *Nucl. Instr. Meth. in Phys. Res. A*, **424**, 9 (1999).

26) A.L. HUTCHESON, and B.F. PLIPS, "A Liquid Scintillator Fast Neutron Double-Scatter Imager", *IEEE Nuclear Symposium Conference Record*, **20-6**, 1126 (2009).

27) J. UHER, "Performance of a Pixel Detector Suited for Slow Neutrons", *Nucl. Instr. Meth. in Phys. Res. A*, **542**, 283 (2005).

28) J. SCHELTON, M. BALZHAUSER, F. HONGESBER, R. ENGLES, and R. REINARTZ, "A New Neutron Detector Development Based on Silicon Semiconductor and ^{6}LiF Converter", *Physics B*, **234-236B**, 1084 (1997).

29) D.S. MCGREGOR, "Design Considerations for Thin Film Coated Semiconductor Thermal Neutron Detectors – I: Basics Regarding Alpha Particle Emitting Neutron Reactive Films", *Nucl. Instr. Meth. in Phys. Res. A*, **500**, 272 (2003).

30) G.J. SAFFORD, T.I. TAYLOR, B.M. RUSTAD, and W.W. HAVNESS, "Precision Determination of the Slow Neutron Absorption Cross Section of ^{10}B", *Physical Review*, 119.4, 1291 (1960).

31) W. CHIEN-SHIUNG, and L.C.L. YUAN, *Methods of Experimental Physics Volume 5 – Part A*, 1st Ed., Academic Press (1961).

32) "Table of Nuclides", Korean Atomic Energy Research Institute (May 2011), available on the Internet at <*http://atom.kaeri.re.kr/cgi-bin/endfform.pl*>

33) J.I. PFEFFER, and S. NIR, *Modern Physcis, An Introductory Text*, 1st Ed., Imperial College Press (2000).

34) D.J. DORSEY, and W. S. CHARLTON, "Measured Energy Spectra of the ^{10}B(n,α)^{7}Li* Recoil De-Excitation in Media of Different Density", *Proc. of the American Nuclear Society Conference*, 725 (2003).

35) X-5 MONTE CARLO TEAM, *MCNP – A General Monte Carlo N-Particle Transport Code, Version 5*, LA-UR-03-1987 , Los Alamos National Laboratory (2003).

36) C. BIAS, *Optimizing the Detection of Neutron from Small-Quantity Weapons-Grade nuclear Materials*, Thesis, Col. State. Univ. (2002).

37) R.T. KOUZES, J.H. ELY, A.T. LINTEREUR, E.R. SICILIANO, and M.L. WOODRING, "BF_3 Neutron Detector Tests", PNNL-1950, Pacific Northwest National Laboratory (2009).

38) J.K. SHULTIS, and D.S. MCGREGOR, "Efficiencies of Coated and Perforated Semiconductor Neutron Detectors", *IEEE Trans. Nuc. Sci.*, **53.3**, 1659 (2006).

39) T.L. ASELAGE, and D. EMIN, *Handbook of Thermoelectrics*, 1st Ed., Sandia National Laboratory (1995).

APPENDIX

A. MCNPX SIMULATIONS

A.1. MCNPX RPM Card

Message: outp=n1.o runtpe=run1.r mctal=heus.m

```
500g HEU Sphere @ 70% enrinchment neutron Spont Fission decay
c Cell Card
c
 29  1  -0.0029  -101                  imp:n=1 $ Air inside hollow sphere
 30  2  -18.9     101 -200              imp:n=1 $ HEU hollow sphere
c    Side dectector definitions
c
1      10 -1.032 -1   2 -4   3 -5  6     imp:n=1  $left side scintillator
2      20 -7.92  -7   1 -4   3 -5  6     imp:n=1  $SS structure between scintillators
3      10 -1.032  7  -8 -4   3 -5  6     imp:n=1  $right side scintillator
4      30 -0.92  18  -2 30 -31 -5  9      imp:n=1  $polyethylene left of scintillator
5      30 -0.92   8 -19 30 -31 -5  9      imp:n=1  $polyethylene right of scintillator
6      30 -0.92   2  -8 30 -14  9 -5      imp:n=1  $polyethylene front of scintillators
7      1  -0.0029   2  -8 -3  14  9  -5          imp:n=1  $air in front of scintillators
8      30 -0.92   2  -8  4 -16  6 -5      imp:n=1  $polyethylene behind scintators
9      30 -0.92   2  -8 17 -31  9 -5      imp:n=1  $polyethylene behind He-3 tubes
10     30 -0.92   2  -8 16 -17 20 -5 +25 +24 +23 +26 +27 +28 imp:n=1 $PE around He-3
tubes
12     20 -7.92  11  -2 15 -13 100 -29    imp:n=1  $leg left
13     20 -7.92 -12   8 15 -13 100 -29    imp:n=1  $right leg
26     1  -0.0029  2 -8  15  -13  100 -29         imp:n=1  $air gap
14     20 -7.92    (-24 34 -5  20):(-34 43 -5):(-34 20 -42) imp:n=1  $he3 tube
15     20 -7.92    (-23 33 -5  20):(-33 43 -5):(-33 20 -42) imp:n=1  $he3 tube
16     20 -7.92    (-26 36 -5  20):(-36 43 -5):(-36 20 -42) imp:n=1  $he3 tube
17     20 -7.92    (-27 37 -5  20):(-37 43 -5):(-37 20 -42) imp:n=1  $he3 tube
18     20 -7.92    (-28 38 -5  20):(-38 43 -5):(-38 20 -42) imp:n=1  $he3 tube
19     20 -7.92    (-25 35 -5  20):(-35 43 -5):(-35 20 -42) imp:n=1  $he3 tube
34     40 .00005377 -34 -43 42           imp:n=1  $he3 tube inside
35     40 .00005377 -33 -43 42           imp:n=1  $he3 tube inside
36     40 .00005377 -36 -43 42           imp:n=1  $he3 tube inside
37     40 .00005377 -37 -43 42           imp:n=1  $he3 tube inside
38     40 .00005377 -38 -43 42           imp:n=1  $he3 tube inside
39     40 .00005377 -35 -43 42           imp:n=1  $he3 tube inside
20     20 -7.92   18 -19 30 -31 -21   5   imp:n=1  $top of box structure
```

```
21     20 -7.92   18 -19 30 -31  -9  29   imp:n=1  $bottom of box structure
22     20 -7.92   18 -19 15 -30  29 -21   imp:n=1  $front of box structure
23     20 -7.92   18 -19 31 -13  29 -21   imp:n=1  $rear of box structure
24     20 -7.92   11 -18 15 -13  29 -21   imp:n=1  $left of box structure
25     20 -7.92   19 -12 15 -13  29 -21   imp:n=1  $right of box structure
27      1 -0.0029 2   -8 16 -17   9 -20   imp:n=1  $air gap under He-3 tubes
28      1 -0.0029 2   -8  3 -16   9  -6   imp:n=1  $air gap under scintillator, and poly
c Car and Dirt Cells
40  50 -7.82 -57 58 54 -55 50 -51         imp:n=1  $solid steel engine block
41  1  -0.0029  59 -60 -63 64 61 -62      imp:n=1  $air inside passenger compart.
42  50 -7.82 51 -52 54 -55 -57 58 #41     imp:n=1  $passenger compartent
43  1  -0.0029 69 -56 59 -60 -63 64       imp:n=1  $air infront of windows
44  80 -2.52 51 -52 55 -68 -57 58 #43     imp:n=1  $glass car windows
45  60 -0.7  -67 61 65 -66 -63 64         imp:n=1  $gasoline located in trunk
46  1  -0.0029 65 -66 -62 67 -63 64 #29 #30          imp:n=1  $air in trunk
47  50 -7.82 52 -53 54 -55 58 -57 #29 #30 #45 #46    imp:n=1  $trunk
48  70 -2.25 -100 -999                  imp:n=1  $ Earth under Car and detector
31  1  -0.0029  -999   #1 #2 #3 #4 #5 #6 #7 #8 #9 #10
        #12 #13 #14 #15 #16 #17 #18 #19 #20 #21 #22 #23
        #24 #25 #26 #27 #28 #34 #35 #36 #37 #38 #39 #29
        #30 #40 #41 #42 #43 #44 #45 #46 #47 #48    imp:n=1 $ Air inside void
99  0   999                           imp:n=0 $ Void

c Surface Cards
c
 101   S   90 -76 49 2     $ Air void in middle
 200   S   90 -76 49 2.42  $ Uranium Sphere
 999   SO  500
c Detector Surface Cards
c
1       px    -5
2       px    -44
3       py    105.065
4       py    109.065
5       pz    232.55
6       pz    141.8
7       px    5
8       px    44
9       pz     73.6
11      px    -63.0
12      px    63.0
13      py    127.86
14      py    100.335
15      py    97.160
```

```
16      py   111.605
17      py   124.685
18      px   -62.365
19      px   62.325
20      pz   142.55
21      pz   238.55
23      c/z  -11.5 118.145 3.5
24      c/z  -24.5 118.145 3.5
25      c/z  -37.5 118.145 3.5
26      c/z  11.5 118.145 3.5
27      c/z  24.5 118.145 3.5
28      c/z  37.5 118.145 3.5
29      pz   71.15
30      py   97.795
31      py   127.225
33      c/z  -11.5 118.145 3.3
34      c/z  -24.5 118.145 3.3
35      c/z  -37.5 118.145 3.3
36      c/z  11.5 118.145 3.3
37      c/z  24.5 118.145 3.3
38      c/z  37.5 118.145 3.3
42      pz   143.05
43      pz   232.05
100     pz    0
c Car Surface Cards
50  px  -135
51  px  -45
52  px  45
53  px  135
54  pz  15
55  pz  83
56  pz  151
57  py  0
58  py  -152
59  px  -41
60  px  41
61  pz  19
62  pz  79
63  py  -4
64  py  -148
65  px  49     $Trunk
66  px  131    $Trunk
67  pz  40     $Gasoline Fill Level
68  pz  153    $top of car
```

```
69  pz  86

c Source Card
c
 MODE N
c
 nps 10000000
c
c Tallies
 F2:N 200
c
c He3 Tallies
 F4:N 34
 FM4 -1 40 103
 F14:N 35
 FM14 -1 40 103
 F24:N 36
 FM24 -1 40 103
 F34:N 37
 FM34 -1 40 103
 F44:N 38
 FM44 -1 40 103
 F54:N 39
 FM54 -1 40 103
c HEU
 SDEF POS=90 -76 49 ERG=d1 RAD=d2 CEL=30
 sp1 -3 0.799 4.903
 si2 2 2.42
c Material Cards
c Air
  m1  7014  0.7
      8016  0.28
      6000  0.02
c Uranium 70% enrichment
  m2  092235 0.7
      092238 0.3
c  Material 10: Plastic Scintillator
m10    1001  0.524
       6000  0.476
c
c  Material 20:  Stainless Steel (SS304)
m20   28000 -0.092078
      26000 -0.686083
      24000 -0.190162
```

```
      25055 -0.020017
      16000 -0.000300
      15031 -0.000450
      14000 -0.010009
       7014 -0.000100
       6000 -0.000801
c
c   Material 30: Polyethylene
m30    6000 -0.85628
       1001 -0.14372
c
c   Material 40: Helium-3
m40    2003  .98
       6000  .002
       1001  .008
       7014  .01
c  Material 50: Carbon Steel
m50    6000  .00196
      26000  .08390
c  7.82 g/cc
c  Material 60: Gasoline
 m60   006012   -1.0
c      004012   .039711191
c      005012   .326714801
c      007012   .081227437
c      008012   .0433213
c      009012   .068592058
c 0.7g/cc
c   Material 70: Earth
m70    1001  .006094
       8016  .043421
      14000  .017390
      13027  .001786
      11023  .000900
      20000  .001958
      26000  .000334
c -2.25
c Material 80: Glass - Simple Silicon Version
m80   14000  -.0903
      11023  -.2527
       8016  -.601
      20000  -.056
c 2.52 g/cc
```

A.2. BF_3 Cloud Chamber MCNPX Deck

```
essage: outp=cut1p99.o runtpe=run1n.r mctal=heus.m ptrac=cut1p99

c Vaccuum environment with B10 to start to learn Ptrac
c
c ========== Cell Cards ==========
11 1 -.00276 -1 imp:n=1 imp:p=1 $ BF3 filled chamber
12 2 -5.33 -3  imp:n=1 imp:p=1 $ Ge Top
13 2 -5.33 -2   imp:n=1 imp:p=1 $ Ge Bott
14 2 -5.33 1 2 3 -4 5 -6 imp:n=1 imp:p=1 $  Ge Side wall
98 3 -0.0029 #11 #14 2 3 -7 imp:n=1 imp:p=1 $ Air surrounding Ge
99 0 7 imp:n=0 imp:p=0 $ imp:a=0 imp:#=0 $ void
c
c

c ========== Surface Cards =======
c
1 RCC 0 0 0 0 0 100 100   $ BF3 filled chamber
2 RCC 0 0 0 0 0 -5 105 $ Bottom Ge plate
3 RCC 0 0 100 0 0 5 105 $ Top Ge Plate
4 CZ 105
5 PZ 0
6 PZ 100
7 SO 300

c ========== Source Cards ========
MODE N p
nps 1000
sdef pos= 0 0 200 vec= 0 0 1 dir=-1 erg=2
c sp1 -3 0.799 4.903
```

```
c phys:p 100 0 0 0 0 -102
c phys:n 100 0 0 -1 -1 1 3
c PTRAC WRITE=all TYPE=a,p,# EVENT=SRC,BNK,COL,TER CELL=50
FILE=ASC MAX=1E9
c cut:# 1E9 0.001
c cut:n 1E9 1.99
c ========== Tally Cards =========
c
c ========= Material Cards ========
c m1 = Boron Carbide with Silicon on the edges
c m1    5010  -.173
m1     009000 0.75
      005010 0.225
       005011 0.025
c m2 = Germanium (abundance in atom percent)
m2  032000.04p -1.0
c m2    032070 0.2123
c      032072 0.2766
c      032073 0.0773
c      032074 0.3594
c      032076 0.744
c m3 Air
m3    7014  -0.7
     8016  -0.28
     6000  -0.02
c m4 Uranium 70% enrichment
m4   092235  -0.70
092238  -0.30
```

A.3. ^{10}B-^{14}Si Efficiency MCNPX Deck

```
Message: outp=18p.o runtpe=run10.r mctal=hd.m

Borated Semiconducter Efficiency tests
c
c Cell Cards
c
1  1  -2.33 -1 2 6 -5 8 -7    imp:n=1 $ Top level of Sn 1mm Thick
2  2  -2.33 -2 3 6 -5 8 -7    imp:n=1 $ Borated Sn, 5mm Thick
3  1  -2.33 -3 4 6 -5 8 -7    imp:n=1 $ Lower level of Sn, 1mm Thick
4  0  -9 #1 #2 #3          imp:n=1 $ Vacumm inside
5  0  9                   imp:n=0 $ Void Region

c Surface Cards
c
1  pz  0.7
2  pz  0.6
3  pz  0.1
4  pz  0.0
5  px  35
6  px  -35
7  py  35
8  py  -35
9  SO  50
c

c Source Card & Data cards
MODE N
c
nps 10000000
c
SDEF POS=0 0 2 ERG=3.0E-8
c
c Tally Cards
c
F4:N 2
FM4 -1 2 107
c
c Material Cards
c
c Silicon, rho = 2.33 g/cc
  m1 014028  -1.0
c
c Borated Sn, B density: 2.34
```

```
  m2 005010  -0.18
     014028  -0.82
c
```

A.4. B_4C MCNPX Thickness Simulations

Message: outp=3cm.o runtpe=run1n.r mctal=heus.m

```
500g HEU Sphere @ 70% enrichment
c New cylindrical shell B4C design. 15 cm thick, 100 cm radius
c Cell Card
c
 29  1  -0.0029  -101                  imp:n=1 $ Air inside hollow sphere
 30  2  -18.9     101 -200              imp:n=1 $ HEU hollow sphere
 50  3  -11.34    200 -201 #30 #29      imp:n=1 $ Lead shell surrounding sphere
 52  4  -1.44     201 -203  #30 #50 #29   imp:n=1 $ Borated-Poly coating
c    New dectector definitions
c
 1  40  -2.31  1 3 -4 -7 100 -503  VOL=1  imp:n=1 $ B4C half cylinder right side
 2  40  -2.31   3 -4 -7 100  503 -502  VOL=1  imp:n=1 $
 3  40  -2.31   3 -4 -7 100  504  502 VOL=1  imp:n=1 $
 4  40  -2.31  1 3 -4 -7 100 -504   VOL=1  imp:n=1 $
 5  40  -2.31  -7 100 -2 5 -6 500  VOL=1 imp:n=1 $ BrC half cylinder left side P-1
 6  40  -2.31  -7 100  5 -6 -500 502  VOL=1 imp:n=1 $ Left Peice 2
 7  40  -2.31  -7 100   5 -6 -501 -502 VOL=1 imp:n=1 $  Left Peice 3
 8  40  -2.31  -7 100 -2 5 -6 501  VOL=1 imp:n=1 $ Left Peice 4
 9  30   -0.92  4 -8 100 -7 1 VOL=1 imp:n=1 $ Right Poly Peice
10 30  -0.92  6 -9  100 -7 -2 VOL=1 imp:n=1 $ Left Poly Peice
c
c Car and Dirt Cells
40  50 -7.82 -57 58 54 -55 50 -51        imp:n=1  $solid steel engine block
41  1  -0.0029  59 -60 -63 64 61 -62      imp:n=1  $air inside passenger compart.
42  50 -7.82 51 -52 54 -55 -57 58 #41     imp:n=1  $passenger compartent
43  1  -0.0029 69 -56 59 -60 -63 64       imp:n=1  $air infront of windows
44  80 -2.52 51 -52 55 -68 -57 58 #43     imp:n=1  $glass car windows
45  60 -0.7  -67 61 65 -66 -63 64         imp:n=1  $gasoline located in trunk
46  1  -0.0029 65 -66 -62 67 -63 64 #29 #30 #50 #52 imp:n=1  $air in trunk
47  50 -7.82 52 -53 54 -55 58 -57 #29 #30 #45 #46 #50 #52  imp:n=1  $trunk
48  70 -2.25 -100 -999                   imp:n=1  $ Earth under Car and detector
31  1  -0.0029  -999  #29 #30 #40 #41 #42 #43 #44 #45
              #9 #10 #46 #47 #48 #50 #52 #1 #2 #3 #4 #5 #6 #7 #8  imp:n=1 $ Air inside
void
99  0   999                          imp:n=0 $ Void
```

```
c Surface Cards
c
 101   S   90 -76 49 2     $ Air void in middle
 200   S   90 -76 49 2.42  $ Uranium Sphere
 201   S   90 -76 49 3     $ Lead Casing
 203   S   90 -76 49 7     $ Polyethylene
 999   SO  10000
c Detector Surface Cards
c
1  py  25
2  py  -177
3  c/z   50 25  100
4  c/z   50 25  103
5  c/z   50 -177  100
6  c/z   50 -177  103
7  pz  170  $ top of car
8  c/z   50 25  113.16
9  c/z   50 -177 113.16
500   P  1 1 0 -127
501   P  -1 1 0 -227
502   PX   50
503   P  1 1 0  75
504   P  -1 1 0 -25
c
c Car Surface Cards
100 pz 0
50  px  -135
51  px  -45
52  px  45
53  px  135
54  pz  15
55  pz  83
56  pz  151
57  py  0
58  py  -152
59  px  -41
60  px  41
61  pz  19
62  pz  79
63  py  -4
64  py  -148
65  px  49      $Trunk
66  px  131     $Trunk
67  pz  40      $Gasoline Fill Level
```

```
68  pz  153     $top of car
69  pz  86

c Source Card
c
 MODE N
c
 nps 10000000
c
c Tallies
c
 F4:N 1
 FM4 -1 40 107
 F14:N 2
 FM14 -1 40 107
 F34:N 3
 FM34 -1 40 107
 F44:N 4
 FM44 -1 40 107
 F54:N 5
 FM54 -1 40 107
 F64:N 6
 FM64 -1 40 107
 F74:N 7
 FM74 -1 40 107
 F84:N 8
 FM84 -1 40 107
 F204:N (1 2 3 4)
 FM204 -1 40 107
 F214:N (5 6 7 8)
 FM214 -1 40 107
c HEU
 SDEF POS=90 -76 49 ERG=d1 RAD=d2 CEL=30
 sp1 -3 0.799 4.903
 si2 2 2.42
c Material Cards
c Air
  m1  7014  -0.7
      8016  -0.28
      6000  -0.02
c Uranium 70% enrichment
  m2  092235 -0.7
      092238 -0.3
c Lead
```

```
  m3  082000 -1.0
c -11.34 g/cc
c Thermo-Reax Boroated poly
  m4  005010 -0.05
      006000 -0.82128
      001001 -0.12232
c -1.4 g/cc
c  Material 10: Plastic Scintillator
m10     1001  -0.524
        6000  -0.476
c
c  Material 20:  Stainless Steel (SS304)
m20    28000 -0.092078
       26000 -0.686083
       24000 -0.190162
       25055 -0.020017
       16000 -0.000300
       15031 -0.000450
       14000 -0.010009
        7014 -0.000100
        6000 -0.000801
c
c   Material 30: Polyethylene
m30     6000 -0.85628
        1001 -0.14372
c
c   Material 40: Boron-Carbide w/ silicon on edges , 2.31g/cc
m40     5010  -.173
        5011  -.02
        6012  -.057
       14028  -.75
c  Material 50: Carbon Steel
m50     28000 -0.092078
       26000 -0.684983
       24000 -0.190162
       25055 -0.020017
       16000 -0.000300
       15031 -0.000450
       14000 -0.010009
        7014 -0.000100
        6000 -0.001901
c  7.82 g/cc
c  Material 60: Gasoline
 m60   006012   -1.0
```

```
c      004012   .039711191
c      005012   .326714801
c      007012   .081227437
c      008012   .0433213
c      009012   .068592058
c 0.7g/cc
c   Material 70: Earth
m70    1001  .006094
       8016  .043421
      14000  .017390
      13027  .001786
      11023  .000900
      20000  .001958
      26000  .000334
c -2.25
c Material 80: Glass - Simple Silicon Version
m80   14000  -.0903
      11023  -.2527
       8016  -.601
      20000  -.056
c 2.52 g/cc
```

A.5. B4C MCNPX Half Cylindrical Shell Detector Deck

Message: outp=n50.o runtpe=run1f.r mctal=heus.m

500g HEU Sphere @ 70% enrichment

```
c New cylindrical shell B4C design. 25 cm thick, 100 cm radius
c Cell Card
c
 29  1  -0.0029  -101                imp:n=1 $ Air inside hollow sphere
 30  2  -18.9     101 -200            imp:n=1 $ HEU hollow sphere
 50  3  -11.34    200 -201 #30 #29    imp:n=1 $ Lead shell surrounding sphere
```

```
 52  4  -1.44     201 -203  #30 #50 #29   imp:n=1 $ Borated-Poly coating
c    New dectector definitions
c
 1  40  -2.31  1 3 -4 -7 100   VOL=1  imp:n=1 $ B4C half cylinder right side
 2  40  -2.31  -7 100 -2 5 -6   VOL=1 imp:n=1 $ BrC half cylinder left side
c
c Car and Dirt Cells
40  50 -7.82 -57 58 54 -55 50 -51         imp:n=1  $solid steel engine block
41  1  -0.0029  59 -60 -63 64 61 -62      imp:n=1  $air inside passenger compart.
42  50 -7.82 51 -52 54 -55 -57 58 #41     imp:n=1  $passenger compartent
43  1  -0.0029 69 -56 59 -60 -63 64       imp:n=1  $air infront of windows
44  80 -2.52 51 -52 55 -68 -57 58 #43     imp:n=1  $glass car windows
45  60 -0.7  -67 61 65 -66 -63 64         imp:n=1  $gasoline located in trunk
46  1  -0.0029 65 -66 -62 67 -63 64 #29 #30 #50 #52 imp:n=1  $air in trunk
47  50 -7.82 52 -53 54 -55 58 -57 #29 #30 #45 #46 #50 #52  imp:n=1  $trunk
48  70 -2.25 -100 -999                  imp:n=1  $ Earth under Car and detector
31  1  -0.0029  -999  #29 #30 #40 #41 #42 #43 #44 #45
                #46 #47 #48 #50 #52 #1 #2  imp:n=1 $ Air inside void
99  0   999                           imp:n=0 $ Void

c Surface Cards
c
 101   S   90 -76 49 2     $ Air void in middle
 200   S   90 -76 49 2.42  $ Uranium Sphere
 201   S   90 -76 49 3     $ Lead Casing
 203   S   90 -76 49 7     $ Polyethylene
 999   SO  1000
c Detector Surface Cards
c
```

```
1  py  25
2  py  -177
3  c/z   -50 25  100
4  c/z   -50 25  115
5  c/z   -50 -177  100
6  c/z   -50 -177  115
7  pz  170  $ top of car
c
c Car Surface Cards
100 pz 0
50  px  -135
51  px  -45
52  px  45
53  px  135
54  pz  15
55  pz  83
56  pz  151
57  py  0
58  py  -152
59  px  -41
60  px  41
61  pz  19
62  pz  79
63  py  -4
64  py  -148
65  px  49      $Trunk
66  px  131     $Trunk
67  pz  40      $Gasoline Fill Level
68  pz  153     $top of car
```

```
69  pz  86

c Source Card
c
 MODE N
c
 nps 10000000
c
c Tallies
c
 F4:N 1
 FM4 -1 40 107
 F14:N 2
 FM14 -1 40 107
c HEU
 SDEF POS=90 -76 49 ERG=d1 RAD=d2 CEL=30
 sp1 -3 0.799 4.903
 si2 2 2.42
c Material Cards
c Air
  m1  7014  0.7
      8016  0.28
      6000  0.02
c Uranium 70% enrichment
  m2  092235 0.7
      092238 0.3
c Lead
  m3  082000 1.0
c -11.34 g/cc
```

```
c Thermo-Reax Boroated poly
  m4  005010 0.05
      006000 0.82128
      001001 0.12232
c -1.4 g/cc
c  Material 10: Plastic Scintillator
m10     1001  0.524
        6000  0.476
c
c  Material 20:  Stainless Steel (SS304)
m20    28000 -0.092078
       26000 -0.686083
       24000 -0.190162
       25055 -0.020017
       16000 -0.000300
       15031 -0.000450
       14000 -0.010009
        7014 -0.000100
        6000 -0.000801
c
c   Material 30: Polyethylene
m30     6000 -0.85628
        1001 -0.14372
c
c   Material 40: Boron-Carbide w/ silicon on edges , 2.31g/cc
m40     5010  .173
           5011  .02
           6012  .057
          14028  .75
```

```
c  Material 50: Carbon Steel
m50     28000 -0.092078
        26000 -0.684983
        24000 -0.190162
        25055 -0.020017
        16000 -0.000300
        15031 -0.000450
        14000 -0.010009
         7014 -0.000100
         6000 -0.001901
c  7.82 g/cc
c  Material 60: Gasoline
 m60    006012    -1.0
c       004012    .039711191
c       005012    .326714801
c       007012    .081227437
c       008012    .0433213
c       009012    .068592058
c 0.7g/cc
c   Material 70: Earth
m70     1001  .006094
         8016  .043421
        14000  .017390
        13027  .001786
        11023  .000900
        20000  .001958
        26000  .000334
c -2.25
c Material 80: Glass - Simple Silicon Version
```

```
m80   14000  -.0903
      11023  -.2527
       8016  -.601
      20000  -.056
c 2.52 g/cc
```

A.6. Doppler Broadening Algorithm Created in the C Programming Language

```
/* Trial doppler broadening program in c*/
#include <stdio.h>
#include <ctype.h>
#include <string.h>
#include <stdlib.h>
#include <math.h>
#include <time.h>

        double doppinfo[6];
        double li_info[6];
        double a_uvw[3];
        double na_solve[3];
        double n_info[6];
        double PtoXZ[3][3];
        double XZtoZ[3][3];
        double ZtoXZ[3][3];
        double XZtoP[3][3];
        double alpharx[3][3];
        double neurx[3][3];
        double gamrx[3][3];
        double gamrz[3][3];
        double malph=4.002602, mli=6.941, mn=1.0086649156;


        double tempstor[4000000],particle_num=0,dopp_count=0;
        char data[4000000],test[100], *EOnumber;

int main(void)
{
```

```
	FILE *rp,*wp,*wp1;
	rp = fopen("thermdatc1","r+");
	wp = fopen("thermoutput6.txt","w");
	wp1 = fopen("alphadata.txt","w");
	fseek (rp, 3, SEEK_END);
	fputc ('z',rp);
	fseek (rp, 0, SEEK_SET);

	fprintf(wp,"Doppler Broadening Algorithm Output Data File \n\n");


	printf("\nCrap Data:\n");

	//********** Attempting to fill crap file with a certain amount of lines *****
	int flag1=0,iter=0;
	char front[1000];
	while(flag1<10){
		front[iter]=fgetc(rp);
		//fread(crap,iter,1,fp);
			//if(*fp=='\n')
			if(front[iter]=='\n')
			flag1++;
  iter++;

	}
	 /* -Eliminating first lines of the code is complete (based off of a set number of
lines.
		-Data will be read into program, converted to double format, then
segmented in an array based off of
		individual particle information. (Every particle will be a temporary array,
none of the information
		will be stored permanently).
		-Search will be performed on the individual particle # to determine if
477.6 kev interaction is in the
		array. If the energy level occurs, math will then be performed based off of
defined array spacing to
		determine doppler broadening.
		- An output file will be generated which tells:
			- # of Doppler broadening cases
			- list broadened energies with particle #
			- percentage of broadened particle interactions*/


	double dopp_time = 0.0, dota_li=0.0, dota_n=0.0;
```

```
	double ecut = 0.01;
	double dotli_nsolved=0, dotli_ngiven=0;
	int p1,cut,p2=0,terminate=0;
	int alphaflag=0,cut2=0;
	double phi=0,theta=0, Ealpha=0,gamm_ang1=0,gamm_ang2=0;
	int ertal=0, z=0;

	while(terminate == 0){

	fread (data, 4000000,1, rp);

	for (int i=0; i<4000000; i++){
	tempstor[i]=0;
	if(data[i] == 'z'){
	printf("The program has finished reading input");
	terminate = 1;
	break;}

	}

	for(int i=0; i<4000000; i++){
		cut=0;
		double freq_gam=0, freq_rel=0, rel_gam=0, beta=0, dopp_fin=0,
cos_angle=0;


		if(i==0){
			tempstor[i]=strtod(data,&EOnumber);
			particle_num=tempstor[0];
			}
		else{
			tempstor[i]=strtod(EOnumber,&EOnumber);
		}

		if(tempstor[i-2]==0.477600){
			p2=i-8;

				for(int k=0; k<7; k++){
					doppinfo[k]=tempstor[p2];  // Assign variable
information to Dopp_info array (energy, position, dir.)
					p2++;
					}
			dopp_count++;
```

```
                    dopp_time = tempstor[i];                    // Locates time (in
shakes) 477.6 KeV particle is created

                  for(int g=(i-1); g>0; g--){     //Going backwards through
input file to find pertinant data
                        if((tempstor[g] == dopp_time) &&   // Test 1.
Looks for same time
                          (tempstor[g-12] == 35.00000) && // Test 2.
Looks to see if its a Heavy Ion
                          (tempstor[g-2] > ecut)){        // Test 3. Looks to
see if its above energy cutoff
                                g=g-2;
                                p1=6;
                                cut=1;
                        }
                        if((tempstor[g] == dopp_time) &&   // Test 1.
Looks for same time
                          (tempstor[g-12] == 1.00000) &&
                          (tempstor[g-17] != dopp_time)){    // Test 2.
Looks to see if its a Neutron
                    g=g-19;
                                p1=6;
                                cut=2;
                                /*if((tempstor[g-17] ==
0.00000)||(tempstor[g-34] == 0.00000)){
                                unscat_tal++;
                                cut2=1;
                                g=g-2;
                                p1=6;
                                cut=2;
                                }
                                else if(cut2==0){
                                z=0;
                                scat_tal++;
                                z=g-19;
                                p1=6;
                                cut=2;
                                }
                                else
                                ertal++;*/
                        }
                        if((tempstor[g] == dopp_time) &&   // Test 1.
Looks for same time
```

```
                                        (tempstor[g-12] == 34.00000)){    // Test 2.
Looks to see if its a Neutron
                                                alphaflag=1;
                                        }
                                        if( cut == 1){          // Assign variable information
to Li_info array (energy, position, dir.)

                                                li_info[p1] = tempstor[g];
                                                p1--;
                                        }
                                        if( cut == 2){          // Assign variable information
to neutron array (energy, position, dir.)
                                                n_info[p1] = tempstor[g];
                                                p1--;
                                        }
                                        if(p1 == 0){
                                        cut=0;
                                        cut2=0;
                                        z=0;}
                                }

        //=================================================================
=======================================
                        //Beginnign of mathematics involving involving alpha, gamma,
neutron angle creation and rotations
                        Ealpha = n_info[6]-li_info[6]+2.31;
                        // Phi = angle between Lithium particle & incident neutron
                        phi = acos((-
2*malph*Ealpha+2*mli*li_info[6]+2*mn*n_info[6])/(2*sqrt(2*mli*li_info[6])*sqrt(2*
mn*n_info[6])));
                        // Theta = angle between Alpha particle & incident neutron
                        theta =
acos(sqrt(2*mn*n_info[6])/sqrt(2*malph*Ealpha)+(2*malph*Ealpha-2*mli*li_info[6]-
2*mn*n_info[6])/(2*sqrt(2*malph*Ealpha)*sqrt(2*mn*n_info[6])));

        //=================================================================
=======================================
                        //*
                        //*
                        //*
                        //*

        //=================================================================
=======================================
```

```
                    //Solving Alpha(u,v,w) Using Neutron and Lithium information,
Then solving neutron u,v,w using calculated alpha and Lithium UVW's
                    // Done by C.O.E. and C.O.M.
                    a_uvw[1] = (n_info[3]*sqrt(2*mn*n_info[6])-
li_info[3]*sqrt(2*mli*li_info[6]))/(sqrt(2*malph*Ealpha));
                    a_uvw[2] = (n_info[4]*sqrt(2*mn*n_info[6])-
li_info[4]*sqrt(2*mli*li_info[6]))/(sqrt(2*malph*Ealpha));
                    a_uvw[3] = (n_info[5]*sqrt(2*mn*n_info[6])-
li_info[5]*sqrt(2*mli*li_info[6]))/(sqrt(2*malph*Ealpha));
                    dota_li =
acos(a_uvw[1]*li_info[3]+a_uvw[2]*li_info[4]+a_uvw[3]*li_info[5])*180/3.14159265;
                    na_solve[1] =
(a_uvw[1]*sqrt(2*malph*Ealpha)+li_info[3]*sqrt(2*mli*li_info[6]))/sqrt(2*mn*n_info[
6]);
                    na_solve[2] =
(a_uvw[2]*sqrt(2*malph*Ealpha)+li_info[4]*sqrt(2*mli*li_info[6]))/sqrt(2*mn*n_info[
6]);
                    na_solve[3] =
(a_uvw[3]*sqrt(2*malph*Ealpha)+li_info[5]*sqrt(2*mli*li_info[6]))/sqrt(2*mn*n_info[
6]);
                    dotli_nsolved =
acos(li_info[3]*na_solve[1]+li_info[4]*na_solve[2]+na_solve[3]*li_info[5])*180/3.141
59265;
                    dotli_ngiven =
acos(li_info[3]*n_info[3]+li_info[4]*n_info[4]+li_info[5]*n_info[5])*180/3.14159265;

          //=============================================================
=========================================
                    //*
                    //*
                    //*
                    //*

          //=============================================================
=========================================
                    /*Creating Rotational Matrices for Alpha, Neutron, Gamma
Particles
                    //1. Initialize all matricies to Zero
                    for (int a=0; a<3; a++){
                              for (int b=0; b<3; b++){
                              PtoXZ[a][b]=0;
                              XZtoP[a][b]=0;
                              XZtoZ[a][b]=0;
                              ZtoXZ[a][b]=0;
```

```
                        alpharx[a][b]=0;
                        neurx[3][3]=0;
                        gamrx[a][b]=0;
                        gamrz[a][b]=0;
                        }
                }

                //2.Rotate to XZ Plane
                PtoXZ[0][0] = PtoXZ[1][1] =
li_info[3]/sqrt(pow(li_info[3],2)+pow(li_info[4],2));
                PtoXZ[2][2] = 1;
                PtoXZ[0][1] =
li_info[4]/sqrt(pow(li_info[3],2)+pow(li_info[4],2));
                PtoXZ[1][0] = -
li_info[4]/sqrt(pow(li_info[3],2)+pow(li_info[4],2));
                //3. Rotate to Z Axis
                XZtoZ[0][0] = XZtoZ[2][2] =
li_info[5]/sqrt(pow(li_info[3],2)+pow(li_info[4],2)+pow(li_info[5],2));
                XZtoZ[1][1] = 1;
                XZtoZ[0][2] =
sqrt(pow(li_info[3],2)+pow(li_info[4],2))/sqrt(pow(li_info[3],2)+pow(li_info[4],2)+pow
(li_info[5],2));
                XZtoZ[2][0] = -XZtoZ[0][2];
                //4.A. Rotate about X Axis-- Alpha particle
                alpharx[0][0] = 1;
                alpharx[1][1] = alpharx[2][2] = cos(theta+phi);
                alpharx[1][2] = -sin(theta+phi);
                alpharx[2][1] = sin(theta+phi);
                //4.B. Rotate about X Axis-- Neutron
                neurx[0][0] = 1;
                neurx[1][1] = neurx[2][2] = cos(phi);
                neurx[1][2] = -sin(phi);
                neurx[2][1] = sin(phi);
                //4.C. Rotate about X Axis-- De-xcitation Photon (random # =
0<#<pi)
                srand (time(NULL));
                gamm_ang1 =
(double)(rand()%100000000)/100000000*3.14159265;
                srand (time(NULL));
                gamm_ang2 =
(double)(rand()%100000000)/100000000*6.28318531;
                //5. Rotate Z to XZ
                for (int a=0; a<3; a++){
                        for (int b=0; b<3; b++){
```

```
                        ZtoXZ[a][b]=XZtoZ[a][b];}
                }
                ZtoXZ[0][2] = -ZtoXZ[0][2];
                ZtoXZ[2][0] = -ZtoXZ[2][0];
                //6.Rotate XZ back to original frame
                for (int a=0; a<3; a++){
                        for (int b=0; b<3; b++){
                        XZtoP[a][b]=PtoXZ[a][b];}
                }
                XZtoP[0][1]=-XZtoP[0][1];
                XZtoP[1][0]=-XZtoP[1][0];

                */

        //=============================================================
=========================================
                //*
                //*
                //*
                //*

        //=============================================================
=========================================
                // Beginning doppler broadening mathematics
                freq_gam = doppinfo[6]*pow(10,6)/4.13566733E-15;
                beta = (sqrt(2*li_info[6]*pow(10,6)*1.60217653E-
19/(6.94*1.660538782E-27)))/3E8;
                cos_angle = li_info[3]*doppinfo[3] + li_info[4]*doppinfo[4] +
li_info[5]*doppinfo[5];
                rel_gam = 1/sqrt(1-beta*beta);
                freq_rel = (freq_gam/rel_gam)*1/(1-beta*cos_angle);
                dopp_fin = (freq_rel*4.13566733E-15)*pow(10,-6);
                /*if(alphaflag==1){
                fprintf(wp,"Particle number[%f]    %f\nPhi: %f\nTheta: %f Alpha
Flag\n\n",particle_num,dopp_fin,phi,theta);
                fprintf(wp,"[%12f]  %12f\n",particle_num,dop_fin
                alphaflag=0;
                }       */

                fprintf(wp,"[%12f]  %12f\n",particle_num,dopp_fin);

              //fprintf(wp,"Ealpha= %f\nNeutron Info: %f %f %f %f %f %f
%f\n",Ealpha,n_info[0],n_info[1],n_info[2],n_info[3],n_info[4],n_info[5],n_info[6]);
```

```
                    //fprintf(wp,"Lithitum Info: %f %f %f %f %f %f
%f\n",li_info[0],li_info[1],li_info[2],li_info[3],li_info[4],li_info[5],li_info[6]);
                        //fprintf(wp,"SUMSQ Neutron: %f
\n",pow(n_info[3],2)+pow(n_info[4],2)+pow(n_info[5],2));
                        //fprintf(wp,"SUMSQ Lithium: %f
\n",pow(li_info[3],2)+pow(li_info[4],2)+pow(li_info[5],2));
                        //fprintf(wp1," %12f  %12f %12f %12f %12f
%12f",particle_num,a_uvw[1],a_uvw[2],a_uvw[3],dota_li,pow(a_uvw[1],2)+pow(a_uv
w[2],2)+pow(a_uvw[3],2));
                        //fprintf(wp1," %12f %12f %12f %12f %12f %12f %12f
%12f\n",na_solve[1],na_solve[2],na_solve[3],dotli_ngiven,n_info[3],n_info[4],n_info[5]
,dotli_nsolved);
                        }



                if((tempstor[i-17]==9000.00000) && // Indexs the particle number by
searching for the flag
                  (tempstor[i-34]==5000.00000) && // and termination interaction #'s,
and performs one last
                  (0 < tempstor[i]-particle_num <= 5)&&
                  (tempstor[i-2] < 1000 )){ // check to determine if the number is close to
its last
                        particle_num = tempstor[i];
                        continue;
                        }

                }


        for(int k=0; k<7; k++){
        printf("Neutron info [%i]: %f\n",k,n_info[k]);
        }
        printf("\n\n Particle # = %f\n # of Broadenings Occuring = %f\n Ratio = %f\n",
particle_num,dopp_count,dopp_count/particle_num);

        printf("\n\n");

}



  printf("\n\n");
```

```
        printf("\n %f %f\n",gamm_ang1,gamm_ang2);
        return 0;
        fclose (wp);
        fclose (rp);


}
```

VITA

Name:	Grant Reid Spence
Address:	Texas A&M University Department of Nuclear Engineering Nuclear Security Science and Policy Institute 3133 TAMU College Station, TX 77843-3133
Email Address:	gspence@tamu.edu grant_spence@hotmail.com
Education:	B.S., Nuclear Engineering, Texas A&M University, 2008 M.S., Nuclear Engineering, Texas A&M University, 2011